Neuroscience

Theta cycle dynamics of spatial representations in the lateral septum

Katarzyna Bzymek, Fabian Kloosterman

Brain & Cognition, KU Leuven, Leuven, Belgium • Neuro-Electronics Research Flanders, Leuven, Belgium • Lead Contact

Reviewed Preprint

Published from the original preprint after peer review and assessment by eLife.

About eLife's process

Reviewed preprint posted
October 9, 2023 (this version)

Posted to bioRxiv
July 19, 2023

Sent for peer review
June 28, 2023

Abstract

Summary

An internal representation of the environment – or map – allows animals to evaluate multiple routes and adapt their navigation strategy to current needs and future goals. The hippocampal formation plays a crucial role in learning a spatial map and using the map for goal-directed navigation. The lateral septum forms a major node for connections between the hippocampus and subcortical brain regions that could link the spatial map to motivation and reward processing centers such as the ventral tegmental area. It is not known, however, how the lateral septum contributes to processing of spatial information and route planning.

In this study we investigated the temporal dynamics of spatial representations in the lateral septum. Neuropixels probes were used to record cellular activity along the dorsal-ventral extent of the lateral septum while rats performed one of two spatial navigation tasks in a Y-maze. The activity of a large fraction of cells was theta rhythmic and a subset of cells showed evidence of being active on alternate theta cycles (theta cycle skipping). Both theta rhythmicity and cycle skipping were strongest in the dorsal lateral septum. Similarly, spatially selective firing was most prominent in the dorsal later septum. Using neural decoding, we show that the lateral septum cell population encodes both the current location and alternatingly the possible future paths within single theta cycles when rats approached the choice point in the maze.

Our data further shows that the alternating expression of spatial representations in the lateral septum is task dependent, such that it is strongest when the task also requires the animals to alternate between rewarded goal arms. These data suggests that task demands and experience shape which representations are activated near a choice point. The lateral septum receives strong input from hippocampal place cells, and while there may be integration and transformation of incoming spatial signals, our findings support the idea that hippocampal spatial representations and their temporal dynamics are conveyed to subcortical projection areas through the lateral septum.

eLife assessment

In this study, the authors present **convincing** evidence to demonstrate theta cycle skipping by individual neurons of the lateral septum, which they then relate to population coding of future trajectories encapsulated by theta cycles. This **valuable** finding furthers our understanding of how the septum conveys navigational information downstream.

Introduction

The ability to navigate the environment in search for food is crucial for the survival of mammals. An internal representation of the environment – or map – allows animals to evaluate multiple routes and adapt their navigation strategy to current needs and future goals. The hippocampal formation plays a crucial role in learning a spatial map and using the map for goal-directed navigation. Route planning strategies during navigation are complex and involve the knowledge of previously visited places and future goals. The lateral septum forms a major node for connections between the hippocampus and subcortical brain regions, including reward processing centers such as the ventral tegmental area (VTA). However, it remains understudied how the lateral septum contributes to processing of spatial information and route planning.

In the hippocampus it has been shown that cell populations represent current locations and upcoming trajectories through spatially selective firing and place cell sequences. These hippocampal spatial representations are expressed cyclically in short bursts that occur at a frequency of approximately 8 Hz (i.e., theta rhythm). Recent studies indicate that during each theta cycle a different environment or path may be represented (Colgin, 2013). In particular, ahead of a binary choice point in a maze, the place cell representations of the two possible future paths are expressed in alternating fashion (Kay et al., 2020), possibly linked to the deliberation about the upcoming choice (Robinson and Brandon, 2021). At the single cell level, this phenomenon is observed as spiking activity "skipping" theta cycles and has been reported beyond the hippocampus in the entorhinal cortex (Brandon et al., 2013), medial prefrontal cortex (Tang et al., 2021) and nucleus reunions (Jankowski et al., 2014).

In recent years, the lateral septum has attracted more attention for its role in memory and spatial navigation (Leutgeb and Mizumori, 2002; Opalka and Wang, 2020; Rizzi-Wise and Wang, 2021; Tingley and Buzsáki, 2018; Trent and Menard, 2010; Wirtshafter and Wilson, 2020, 2019). The lateral septum is predominantly composed of GABAergic spiny neurons (Rizzi-Wise and Wang, 2021). It receives strong input from hippocampal subfields CA3 and CA1 that is organized topographically along the dorsal-ventral axis (Wirtshafter and Wilson, 2021), and it projects to the hypothalamus and VTA. Given the central position of the lateral septum in the network linking the hippocampus to subcortical brain regions for motivation and reward processing, the question arises if and how hippocampal spatial representations and their temporal dynamics are relayed and transformed within this circuit.

The activity of lateral septum neurons is modulated by the hippocampal theta rhythm (Tingley and Buzsáki, 2018; Wirtshafter and Wilson, 2019) and some studies suggest that the lateral septum may contribute to hippocampal theta generation (Monmaur et al., 1993; Pedemonte et al., 1998; van der Veldt et al., 2021). A few studies have reported place cell-like activity in the lateral septum (Tingley and Buzsáki, 2018; Wirtshafter and Wilson, 2020, 2019), as well as activity related to self-motion signals including running speed, acceleration and movement direction (van der Veldt et al., 2021; Wirtshafter and Wilson, 2020; Zhou et al., 1999). A

subset of lateral septum neurons have spatial coding properties that remain stable over multiple days, suggesting an involvement in long term spatial memory (van der Veldt et al., 2021). One study (Tingley and Buzsáki, 2018) found a lack of spatial rate coding in the lateral septum and instead reported a place coding by specific phases of the hippocampal theta rhythm (Rizzi-Wise and Wang, 2021).

In this study we investigated the temporal dynamics of spatial representations in the lateral septum. Neuropixels probes were used to record along the dorsal-ventral extent of the lateral septum while animals performed a spatial navigation task. The activity of a large fraction of cells was theta rhythmic and a subset of cells showed evidence of theta cycle skipping. Both theta rhythmicity and cycle skipping were most prominent in the dorsal lateral septum. Using neural decoding, we show that the lateral septum cell population encodes both the current location and alternatingly the possible future paths within single theta cycles. Taken together, these findings indicate that hippocampal spatial representations and their temporal dynamics are conveyed to subcortical projection areas.

Results

Neural recordings across different septal subregions during execution of alternation/switching task

To characterize the temporal and spatial coding properties of neurons in the lateral septum (LS), we recorded activity along the dorsal-ventral extent of the LS spanning both dorsal (LSD) and intermediate (LSI) subregions (**Figure 1A, B**; **Figure 1 - figure supplement 1**) in four rats. Animals were trained to run on a Y-maze (**Figure 1C**) and shuttle between a home (H) platform and left (L)/right (R) goal arms as part of a spatial alternation task (**Figure 1D, left**) or switching task (**Figure 1D, right**). Sessions chosen for analysis were those in which the animals were familiar with the task and performed over 75% correct choices (spatial alternation task) or at least one successful arm switch (switching task). Outbound journeys that started at the home platform and ended in one of the goal arms were analyzed separately from inbound journeys in which rats ran from the goal arms towards home (**Figure 1C, right**). We analyzed a total of 1227 cells across 12 sessions from four animals (**Table 1**). The mean firing rate of LSD cells was lower than the mean firing rate of cells located in LSI (**Figure 1E**). An example of spiking activity on one outbound journey is shown in **Figure 1F**.

Strong theta rhythmicity in the lateral septum

Lateral septal neurons receive rhythmic theta frequency (6-10 Hz) input from the hippocampus and their firing is locked to theta oscillations in the local field potential (Bender et al., 2015; Tingley and Buzsáki, 2018; Wirtshafter and Wilson, 2019). We first characterized the theta rhythmic firing pattern of lateral septum neurons during outbound and inbound journeys in our dataset. Theta rhythmicity was present in the spiking auto-correlogram of cells in both LSD and LSI subregions (**Figure 2A**). To quantify the level of theta rhythmicity, we computed the relative theta peak power in the spectrum of binned spike trains (**Figure 2B**) and classified cells as theta rhythmic if the relative peak power was significantly higher than the value expected from locally jittered spike trains (see Methods for details; **Figure 2B**). More than half of the cells in LSD and LSI showed significant theta rhythmic firing (LSD: 56.9%, LSI: 59.2%; see **Figure 2 - figure supplement 1A**). The firing rate of theta-rhythmic cells was significantly higher than the firing rate of non-rhythmic cells for both subregions (**Figure 2 - figure supplement 1B**). The strength of theta rhythmicity varied along the dorsal-ventral axis of LS, such that cells located more

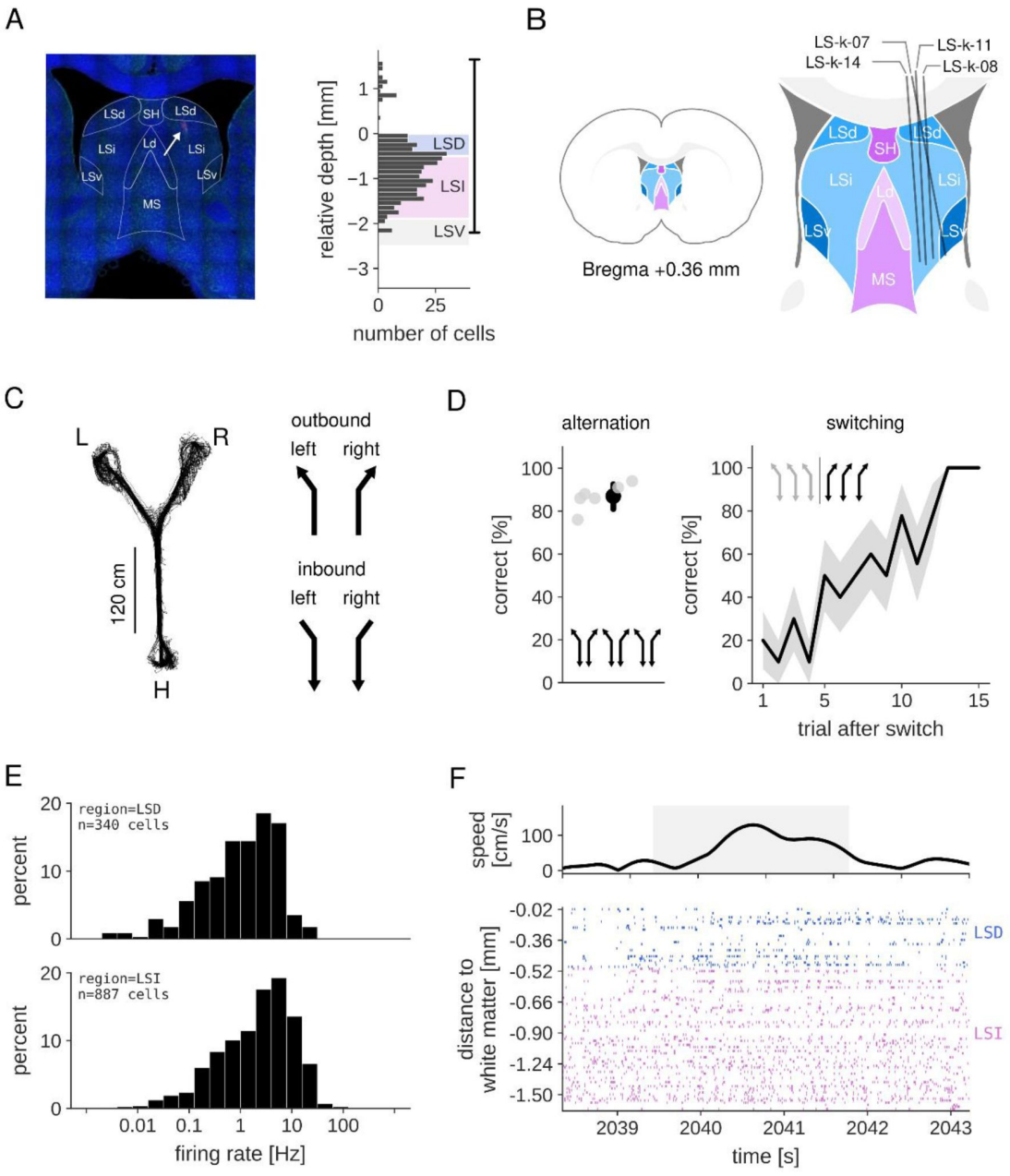

Figure 1.

Neural recording in the lateral septum.

(A) Left: coronal brain slice showing part of the Neuropixels probe trajectory (white arrow) in the lateral septum (animal LS-k-7). Right: the number of recorded cells along the probe shank for one recording session in the same animal. Depth is measured relative to the white matter above the lateral septum. Vertical line at the right indicates the span of the recorded electrodes on the probe. (B) A schematic overview of the probe tracks in all animals, projected onto a single coronal slice at 0.36 mm anterior to Bregma. (C) Left: example tracked position from a session in which the animal performed the alternation task on the Y-maze. Right: definition of outbound and inbound trajectories. (D) Left: the percentage of correct visits for all alternation task sessions. Gray dots represent individual sessions, black dot represents median and 95% confidence interval across sessions. Right: the mean percentage of correct visits for 15 trials after a reward switch for all switching task sessions. (E) Log-distribution of mean firing rates for LSD (top) and LSI (bottom) cells in all analyzed sessions. Overall mean±sem firing rate: LSD 2.52±0.18 Hz, LSI 5.21±0.24 Hz. (F) Example behavior and spiking activity in a single session during one outbound journey. Top: running speed. Gray region marks the outbound journey. Bottom: spike raster plot of all cells recorded in LSD and LSI.

Animal	Task		Brain region LSD		Brain region LSI	
	alternation	switching	number of cells	mean rate [Hz]	number of cells	mean rate [Hz]
LS-k-7	•		29	4.70	69	5.25
	•		25	3.43	79	4.16
	•		34	3.62	92	4.56
LS-k-8		•	22	1.90	87	5.61
		•	32	2.40	88	4.53
	•		29	1.55	72	5.25
LS-k-11		•	32	1.21	60	8.45
		•	14	1.16	62	4.17
		•	31	1.93	47	6.53
LS-k-14		•	30	1.94	56	5.14
	•		32	2.88	78	5.23
	•		29	2.84	93	4.96
Total	N=6	N=6	N=340	2.52	N=887	5.21

Table 1

Overview of data.

An overview of all analysed sessions from four animals performing either an alternation task or a switching task, with the number of recorded cells and corresponding mean firing rate for septal subregions LSD and LSI.

dorsally had higher relative theta peak power than cells located ventrally (**Figure 2 - figure supplement 1C**). As a consequence, the relative theta peak power was significantly higher for cells in LSD as compared to cells in LSI (**Figure 2 - figure supplement 1D**).

Theta cycle skipping in lateral septal cells is trajectory specific

At binary choice points in the environment, the activity of hippocampal place cell ensembles upstream of the LS switches between two alternative future paths in phase with the local theta rhythm (Kay et al., 2020). At the single cell level, this switching is evident from cells being activated at alternating theta cycles and increased rhythmicity at half theta frequency (i.e., "theta cycle skipping"). Here we asked if neurons in LS display similar cycle-to-cycle dynamics that is consistent with theta cycle skipping behavior.

In a subset of LSD and LSI cells we found evidence of enhanced rhythmicity at half theta frequency (i.e., time lag of ~250 ms) in the spiking auto-correlogram (**Figure 2A**) that corresponds to a peak in the spectrum around 4 Hz (**Figure 2B**). For each cell, we computed a cycle skipping index (CSI) as the normalized amplitude difference between the first and second theta-related peaks in the spiking auto-correlogram (Brandon et al., 2013; Kay et al., 2020). Given variability in the theta frequency over time, the auto-correlogram of most cells takes the form of a dampened oscillation and the expected CSI value for a purely theta-rhythmic (non-skipping) cell is slightly negative. CSI values were compared to a shuffle distribution that was constructed from locally jittered spike trains that maintained theta rhythmicity but destroyed cycle skipping (**Figure 3A**; see Methods for details). CSI values were considered statistically significant if the Monte-Carlo p-value obtained from the shuffle procedure was smaller than 0.05 (**Figure 3B**).

We first focused on the properties of theta cycle skipping cells and noticed that in the spiking auto-correlogram the enhanced rhythmicity at half theta frequency was dependent on the type of trajectory (**Figure 3C**). In our further analysis, we divided journeys into four different trajectory categories: inbound left, inbound right, outbound left, and outbound right, and quantified theta cycle skipping only for cells that had at least 50 spikes for one or more trajectory types. We found that 39.6% (107/270) of cells in LSD and 32.4% (247/763) of cells in LSI had significantly higher CSI values than expected by chance on at least one of the trajectories (see **Figure 3 - figure supplement 1A**). As expected, the population of cycle skipping cells overlapped to a large extent with the population of theta rhythmic cells (**Figure 3D**). Cells located more dorsally in the LS on average showed higher CSI values than cells located in the ventral part (**Figure 3 - figure supplement 1B**). Consequently, the mean CSI values were significantly higher for cells in LSD, compared to LSI (**Figure 3 - figure supplement 1C**).

Next, we looked more closely at the selectivity of theta cycle skipping based on the type of trajectory. We noticed for most of the cells (55.4%, 196/354), the theta cycle skipping behavior happens on only one type of trajectory (**Figure 3E**). For another population of cells (22.0%, 78/354) the skipping behavior occurs on a combination of two trajectories: outbound, inbound, left, or right. This type of trajectory selectivity was consistent across both septal subregions (**Figure 3 - figure supplement 2**).

Given the trajectory dependence of cycle skipping activity, we next asked if cycle skipping occurred at specific locations on the track. The spiking patterns of individual cells showed half-theta periodicity at certain locations on the track that was variable from journey to journey (**Figure 4**). To quantify the spatial preference for theta cycle skipping in individual cells, auto-correlations and CSI values were computed for spiking activity on multiple overlapping 60 cm-long subsections of the track along each of the trajectories (**Figure 5A**; see examples in **Figure 5 - figure supplement 1** and **Figure 5 - figure supplement 2**). This analysis was only carried out for cell-trajectory combinations for which significant cycle skipping was already established

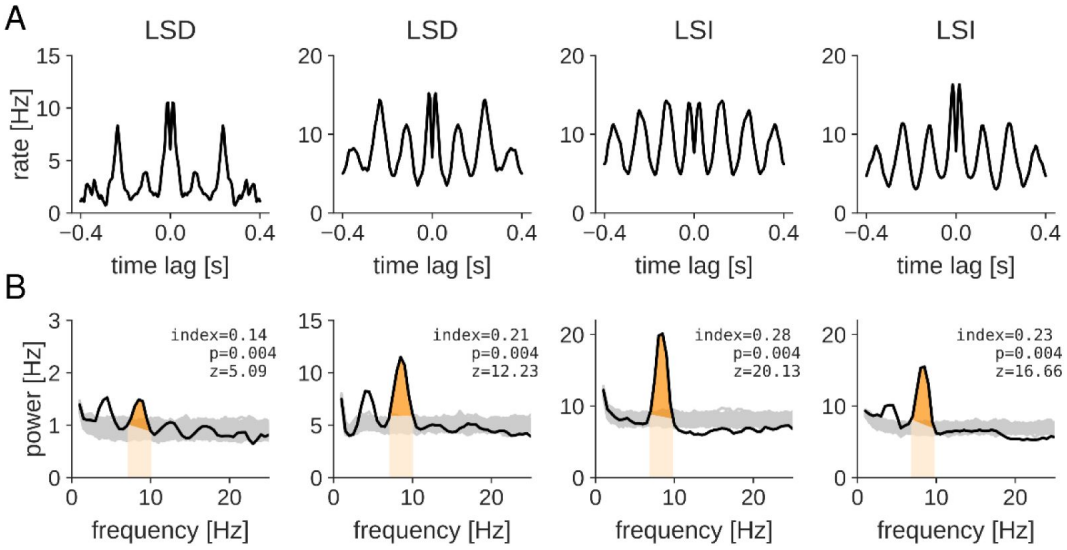

Figure 2.

Theta rhythmicity and theta cycle skipping in lateral septum cells.

(A) Spiking auto-correlograms of four example cells in LSD and LSI that show clear rhythmicity at theta frequency. (B) Power spectra of (binned) spike trains for the same cells as in panel A. Gray traces represent spectra of locally shuffled spike trains. Theta peak index is computed as the normalized difference between theta peak power (dark orange) and theta base power (light orange). Inset shows values for theta peak index, Monte-Carlo p-value an z-scored index relative to shuffle distribution.

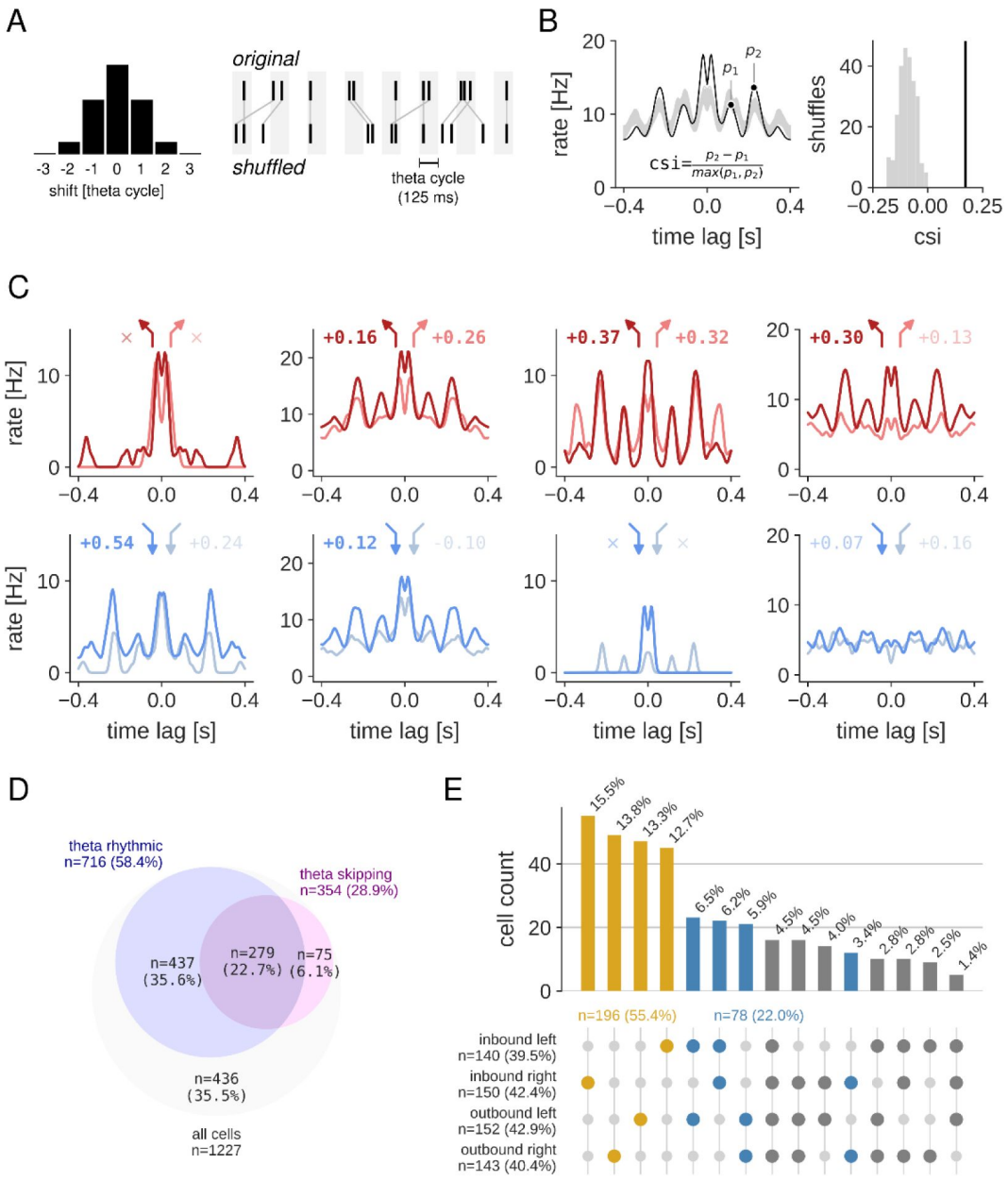

Figure 3.

Theta cycle skipping is trajectory specific.

(A) Local shuffling procedure to compute significance of cycle skipping effect in single cells. Each spike is randomly shifted by a multiple of the theta cycle (fixed to 125 ms) according to a normal distribution (shown on the left). (B) Left: example spiking auto-correlogram of original spike train (black line) and shuffled spike trains (gray). A cycle skipping index (CSI) is computed as the normalized difference between the first and second theta-related peaks. Right: distribution of CSI values for 250 shuffled spike trains (gray) and CSI value of the original spike train (black line). (C) Spiking auto-correlograms of four example cells in LSD and LSI separately for each of the four kinds of journeys (top: outbound journeys, bottom: inbound journeys). Legend at the top of each plot indicates for each journey type the CSI value (printed in bold for significant CSI values). The symbol × means that a cycle skipping index could not be computed because of low number of spikes. From left to right, the first and fourth cell show significant cycle skipping only for a single trajectory type (respectively, inbound left and outbound left). The second cell shows significant cycle skipping for three trajectory types, and the third cell for both outbound trajectories. (D) Venn diagram showing overlap of cell populations with significant theta rhythmicity and theta cycle skipping. (E) Histogram of the number of cells with a significant cycle skipping index for all possible journey combinations. Note that for most cells (55.4%; yellow) cycle skipping occurs only on a single journey type. For another population of cells (22.0%; blue), cycle skipping occurs on outbound, inbound, left, or right journeys.

using all spikes along the full trajectory. Individual cells showed cycle skipping mainly around the choice point and in the goal arm on outbound and inbound trajectories, even if the cell was also active on other parts of the track (e.g., see 1st and 4th example in **Figure 5 - figure supplement 1**).

On average, across all cell-trajectory combinations, CSI values on outbound journeys were high right before the choice point and in the goal arm (**Figure 5A, left**). On inbound journeys, CSI values were high in the goal arm leading up to the choice point (**Figure 5A, right**). These higher CSI values corresponded to a higher percentage of cell-trajectory combinations with significant cycle skipping as compared to jittered spike trains (**Figure 5B**). These data show that cycle skipping occurs specifically around the choice point and in the goal arm in both run directions.

Spatial coding in the lateral septum

Given that theta cycle skipping cells in lateral septum are highly trajectory specific, we next investigated spatial properties of lateral septal cells and the relation to cycle skipping dynamics. In previous studies it was shown that lateral septal neurons convey spatial information (Tingley and Buzsáki, 2018; Wirtshafter and Wilson, 2020, 2019), although less than hippocampal neurons. Consistent with these studies, the firing rate of a large fraction of LS cells in our dataset was non-uniform across position in the Y-maze with spatial information higher than expected by chance (**Figure 6 - figure supplement 1**; percent spatially modulated cells, LSD: 75.0%, LSI: 59.4%). Even so, spatial information was generally low (<1 bit/spike), indicating only modest spatial tuning that was stronger for cells in LSD as compared to LSI (**Figure 6 - figure supplement 1**).

Spatial tuning curves for each neuron were computed separately for the four different trajectories (i.e., outbound left/right and inbound left/right; **Figure 6A**). We observed that a subset of septal neurons showed trajectory-specific activity, with cells firing differentially on the left/right goal arms (**Figure 6A, top row**) or in the outbound versus inbound journeys **Figure 6A, bottom row**).

We quantified the goal arm selectivity for outbound and inbound journeys separately for active cells with a mean firing rate higher than 1 Hz on at least of the goal arms. Overall, a high percentage of all cells were active on one or both of the goal arms (percentage of cells, outbound: 70.5% (865/1227), inbound: 67.1% (823/1227)). Of the active cells, the fraction that showed a significantly higher firing rate on one of the goal arms was higher in the outbound direction as compared to the inbound direction (**Figure 6B**; outbound: 50.4% (436/865), inbound: 29.3% (239/823)).

When split by subregion, a higher percentage of cells in LSI were active on the goal arms than cells in LSD (percentage of cells, outbound: LSD 60.6% (206/340), LSI 74.3% (659/887), inbound: LSD 57.4% (195/340), LSI 70.8% (628/887)). However, of the population of goal arm active cells, a higher fraction of cells in LSD than in LSI was selective for one of the goal arms (i.e., cells fired at a higher rate on one of the goal arms), and higher in outbound journeys as compared to inbound journeys for both brain regions (**Figure 6 - figure supplement 2A,D**). Within the population of goal arm selective cells, the relative spiking rate difference between the left and right arms was higher for cells located more dorsally in the LS for both outbound and inbound journeys (**Figure 6 - figure supplement 2B,E**). This gradient of goal arm selectivity resulted in a significant higher selectivity for goal-arm selective cells in LSD than in LSI (**Figure 6 - figure supplement 2C,F**). In contrast to the strong goal-arm specific activity, lateral septal neurons showed little prospective or retrospective coding on the stem of the Y-maze (**Figure 6 - figure supplement 3**).

We next analyzed the relative firing rate difference in outbound and inbound trajectories (i.e., directionality) of LS neurons. Of the cells that were active with a mean rate above 1 Hz in either outbound or inbound direction (percentage of cells, 70.5% (865/1227)), approximately half showed

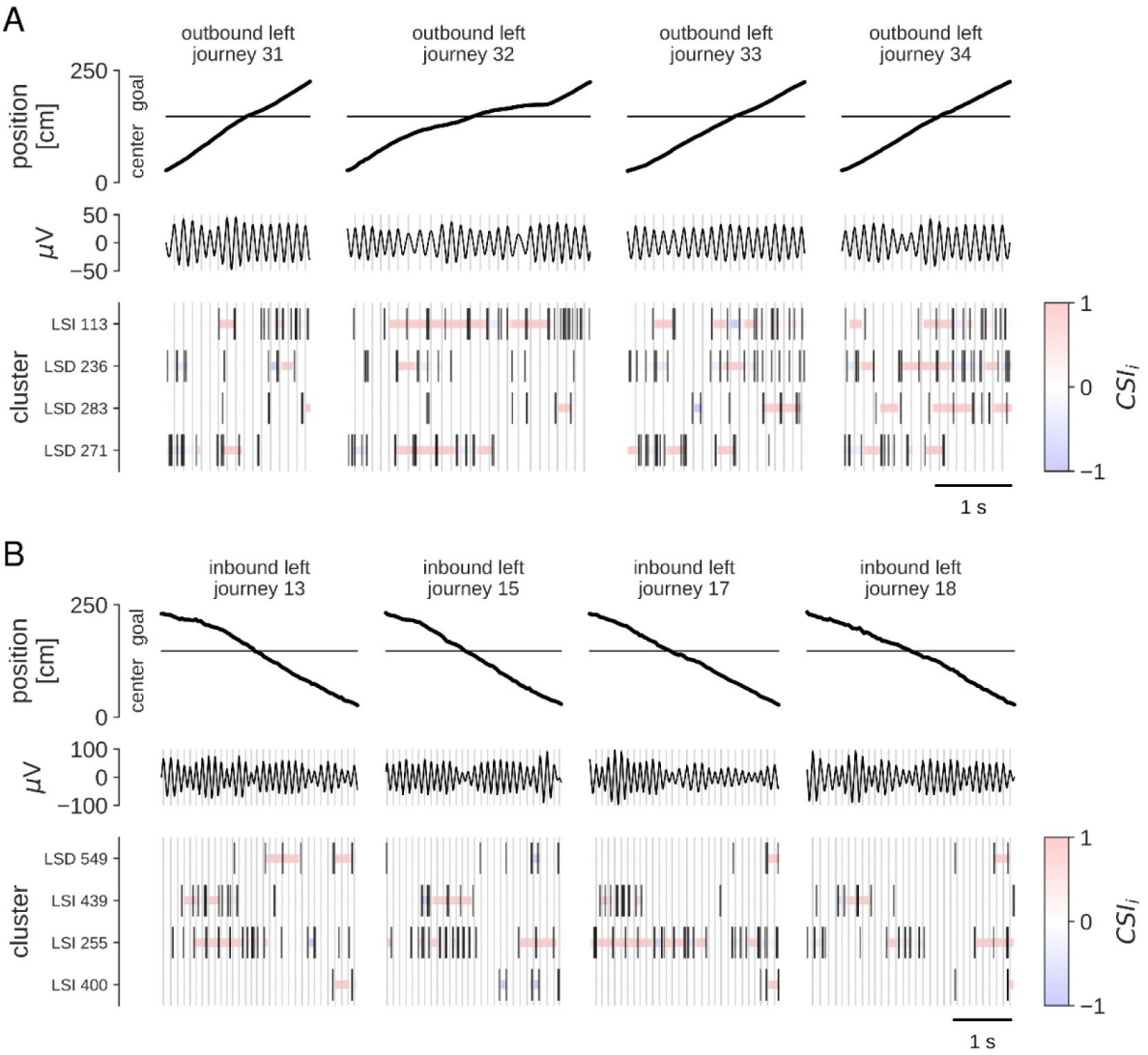

Figure 4.

Examples of theta cycle skipping during single journeys.

(A) Spike raster plots (bottom) of selected lateral septum cells (animal LS-k-7) during four outbound journeys to the left goal. Top: position of the animal represented as the distance between home and goal. Middle: local field potential in the LSD filtered in the theta band (6-10 Hz). Vertical grey lines indicate times of peaks in theta oscillation. Bottom: for each cell, spike times (black lines) and an instantaneous estimate of cycle skipping (CSI_i, red indicates relative excess of spike intervals in range 0.2- $0.\bar{3}$ seconds). (B) Same as in for selected cells (animal LS-k-8) during four inbound journeys starting from the left goal.

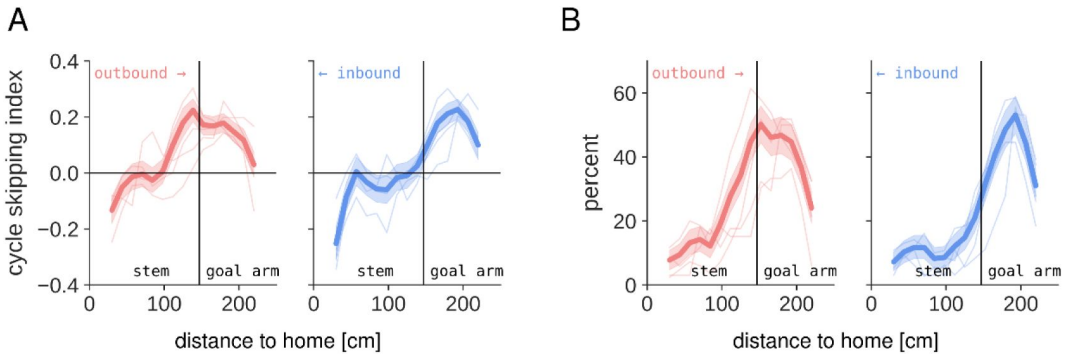

Figure 5.

Theta cycle skipping occurs on approach to the choice point and in the goal arms.

(A) Average CSI value as a function of location along outbound (left) and inbound (right) trajectories. Thick lines represent average across all analyzed cells and trajectories to/from left and right goals. Thin lines represent average for individual animals. (B) Same as (A) but for the percent of analyzed cells and trajectories with significant cycle skipping.

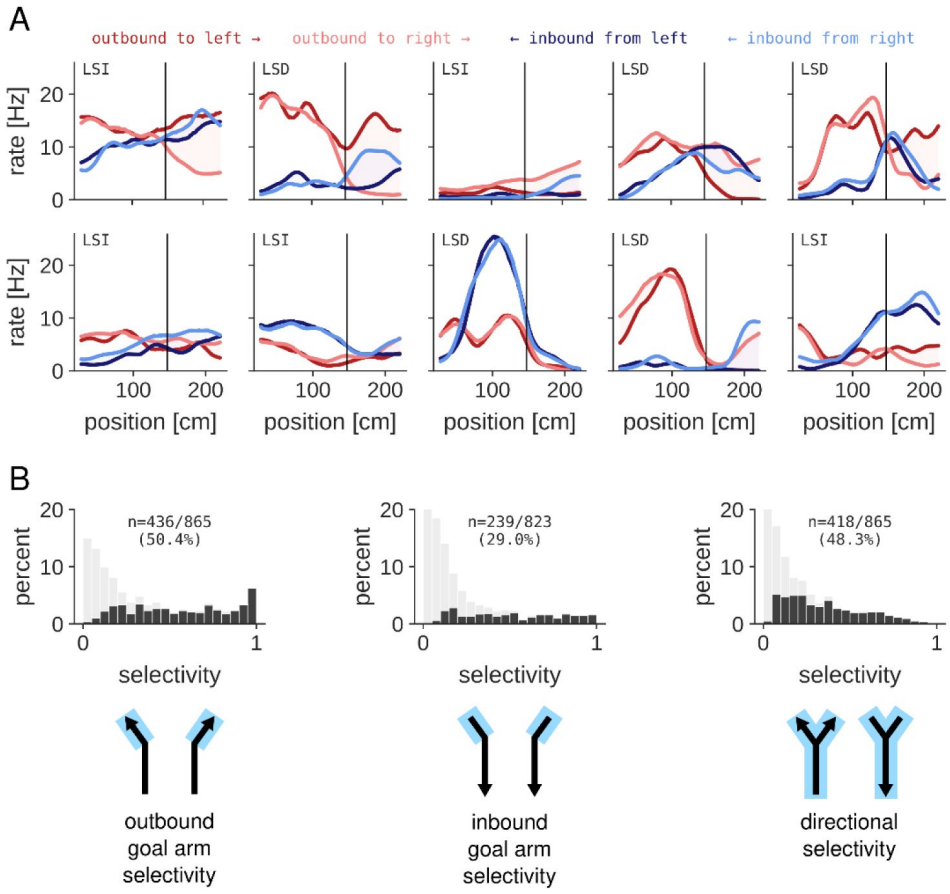

Figure 6.

Spatial coding in the lateral septum.

(A) Spatial tuning curves for 10 example neurons in LSD and LSI for the four different trajectories. (top: trajectory-specific neurons firing differentially on the left/right goal arms, bottom: direction-specific neurons firing differentially on the outbound versus inbound journeys). (B,C) Distribution of outbound (B) and inbound (C) goal arm selectivity of all analyzed neurons in LSD and LSI. Light orange: full distribution of all cells. Dark orange: highlighted part of the distribution that represent cells with significant goal arm selectivity (Monte-Carlo p-value < 0.01). (D,E) Values of outbound (D) and inbound (E) goal arm selectivity index increases for cells located closer to the white matter. Dots represent individual cells with significant goal arm selectivity index from all sessions and animals. Black line and shaded region represent linear fit and 95% confidence interval. (F,G) Mean value of outbound (F) and inbound (G) goal arm selectivity index is significantly higher in LSD as compare to LSI (mean±sem goal arm selectivity, outbound: LSD 0.75±0.02, LSI 0.49±0.02, two-sided two-sample t-test, $t(434)=9.40$, $p=3.1\times10^{-19}$; inbound: LSD 0.61±0.03, LSI 0.44±0.02, two-sided two-sample t-test, $t(237)=4.65$, $p=5.6\times10^{-6}$).

directional tuning (**Figure 6B**; percentage of cells, 48.3% (418/865)). Similar to goal arm selectivity, we found more direction selective cells in LSD as compared to LSI (**Figure 6 - figure supplement 2G**). Within the population of direction selective cells, the strength of directionality depended on the cell location along the dorsal-ventral axis (**Figure 6 - figure supplement 2H**). Consequently, the mean directionality was significantly higher in LSD than LSI (**Figure 6 - figure supplement 2I**. The directional and goal arm selective neurons formed discrete but partially overlapping cell populations (**Figure 6 - figure supplement 2J,K**).

Stronger position and direction coding in the dorsal lateral septum cell population

Given the spatial coding properties of individual LSD and LSI cells, we tested how well both position and running direction were represented in the population of cells. For this, we performed neural decoding analysis on outbound and inbound journeys and quantified the decoding error (**Figure 7**). Overall, there was a good correspondence between the estimated and true position and running direction when using all LSD and LSI cells for decoding (**Figure 7A,B**). The median error for position ranged from 6.0–18.0 cm across sessions (mean of all sessions: 10.2 cm; **Figure 7C**) and the percentage correct for running direction ranged from 86.9%-96.2% (mean of all sessions: 91.5%; **Figure 7C**).

We next looked at position and direction coding separately for the populations of LSD and LSI cells. Decoding performance was similar for the LSD and LSI cell populations, and somewhat worse than the performance when both cell populations were combined (**Figure 7C**). Given that the number of LSD cells in our dataset is approximately half of the number of LSI cells, these results are consistent with stronger spatial coding in LSD. Indeed, when decoding performance was characterized as a function of the number of cells, fewer LSD cells than LSI are required for a similar performance level (**Figure 7 - figure supplement 1**).

Theta-cycle dynamics of lateral septum spatial representations

We next analyzed the decoded spatial representations in the population of lateral septum cells at the timescale of theta cycles. For this, we used the same encoding model as before, but decoding was performed in overlapping 50 ms time bins. As expected, spatial and directional estimates are noisier at this finer timescale, but still largely reflect the behavior of the animal (**Figure 8**). In addition, we observed non-local spatial representations of the two maze arms where the animal was not located, most strongly when animals ran towards the choice point (outbound on the stem, or inbound on the goal arms; see **Figure 8 - figure supplement 1**). To analyze the temporal dynamics of the local and non-local spatial representations, we first computed the time course of the total posterior probability $P_{arm}(t)$ assigned to each of the three maze arms (**Figure 8, bottom**). Next, auto- and cross-correlations of these signals were computed separately for journeys towards the choice point in either the stem (**Figure 9A**) or left/right goal arms (**Figure 9B**). As animals ran on the stem towards the choice point, the local spatial representations were strongly theta modulated (**Figure 9** **Figure 8A, top**). In contrast, non-local spatial representations of the goal arms were modulated at half theta frequency (**Figure 9A, second plot from top**), consistent with theta cycle skipping of spiking activity at the single cell level. Cross-correlation of the local and non-local spatial representations showed an out-of-phase theta-rhythmic relationship (**Figure 9A, third plot from top)**, which is consistent with a model in which half of the theta cycle is used for representing the current location and the other half for scanning potential future locations. Finally, cross-correlation between the spatial representations of the two goal arms showed a peak at ~125 ms (**Figure 9A, bottom**), consistent with an alternating representation of each goal arm.

The pattern is generally similar for journeys towards the choice point in the goal arms (**Figure 9B**), albeit less pronounced. However, no pronounced theta scale dynamics of the spatial representations were observed when animals ran toward the reward (and away from the choice

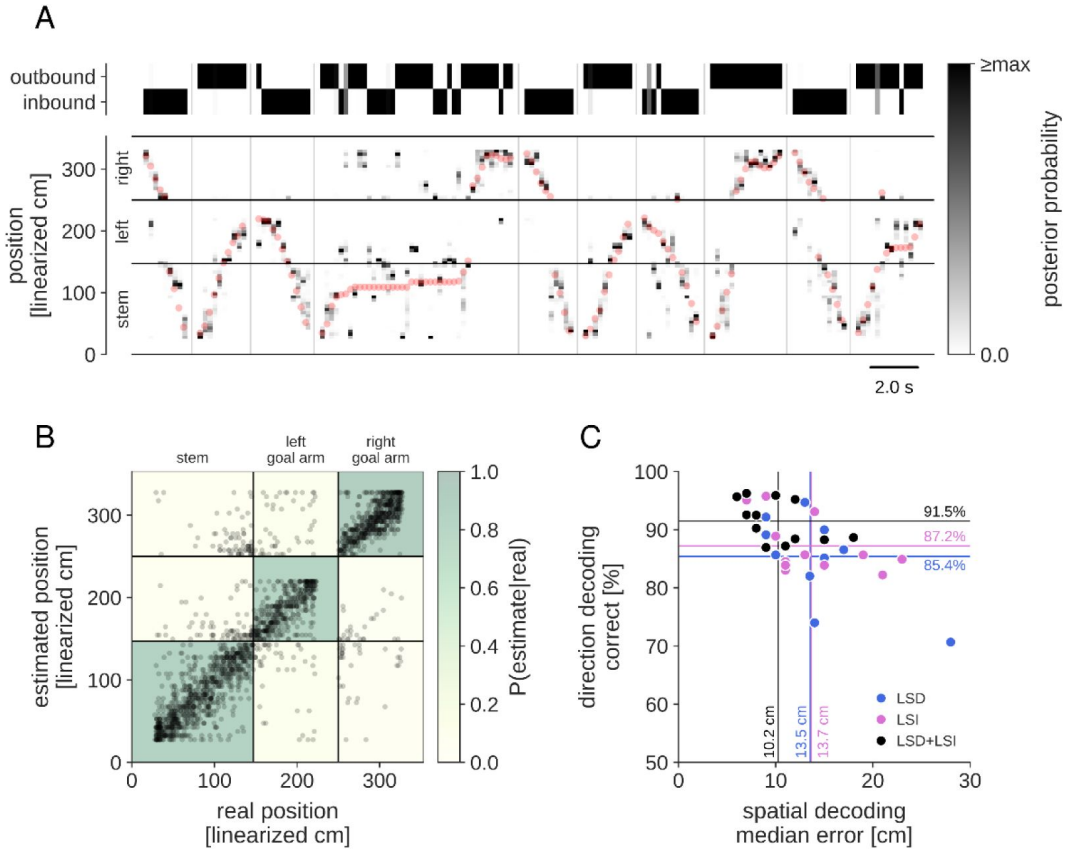

Figure 7.

Position and direction coding in the lateral septum cell population.

(A) Example result of decoding run direction (top) and position (bottom) for a single dataset (animal LS-k-7). For both direction and position, the marginal posterior probability is shown in grey scale. Position on the track is "linearized" and the horizontal black lines indicate the extent of the three maze sections: stem (bottom), left goal arm (middle) and right goal arm (top). Note that the home platform and goal platforms are excluded from the encoding model, and no decoding is performed for the time that the animal spent at the platforms. A sequence of ten outbound/inbound journeys is shown (separated by vertical lines). Red dots indicate the true position of the animal on the track. (A) Confusion matrix of the decoding result for the same session as in (A). Each dot represents a single maximum a posteriori position estimate in a 200 ms time bin during run periods (speed > 10 cm/s) in outbound/inbound journeys. The diagonal structure indicates good correspondence between estimated and true positions. The color map in the background shows the confusion matrix for decoding the three maze sections. For this session, median position error is 12.0 cm and 94.7% of direction estimates are correct. (C) Spatial and direction decoding performance for all sessions using all LSD and LSI cells combined or using only cells in LSD or LSI. Vertical and horizontal lines indicate mean performance across sessions.

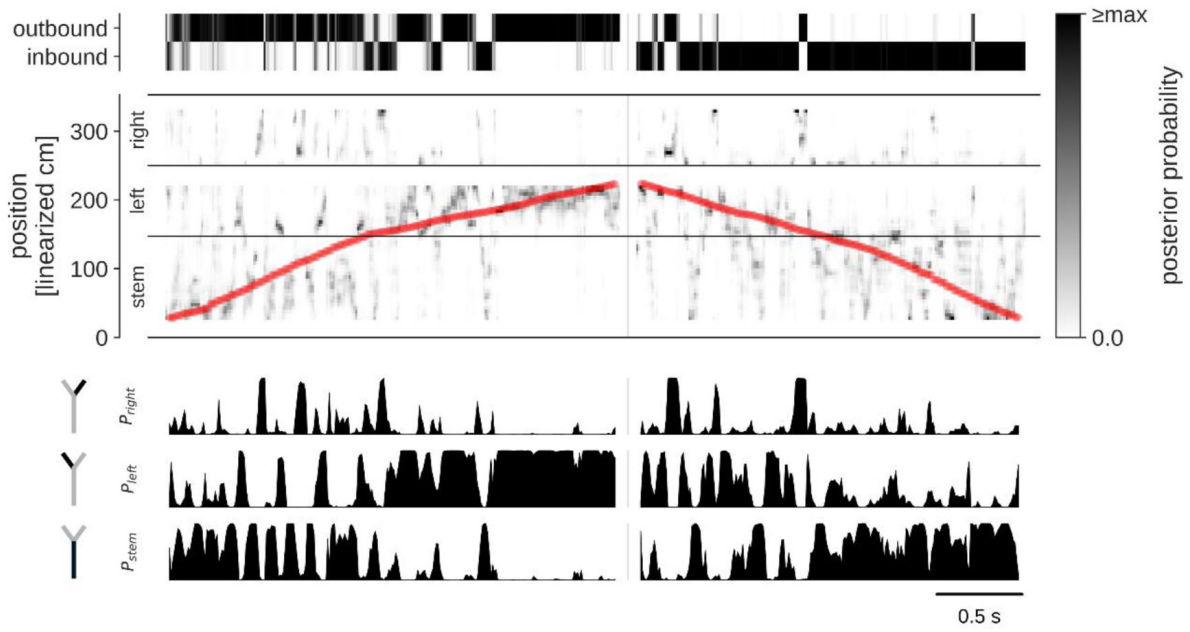

Figure 8.

Neural decoding of theta-scale dynamics in lateral septum.

(A) Example result of decoding run direction (outbound or inbound; top) and position (middle) at fine time scale (20 ms) for a single dataset (animal LS-k-7). For both direction and position, the marginal posterior probability is shown in grey scale (black represents probability of 1 for direction, and ≥0.25 for position). Position on the track is "linearized" and the horizontal black lines indicate the extent of the three maze sections: stem, left goal arm and right goal arm. Note that the home platform and goal platforms are excluded from the encoding model, and no decoding is performed for the time that the animal spent at the platforms. A sequence of one outbound and one inbound journey is shown (separated by vertical lines). Red dots indicate the true position of the animal on the track. Bottom: time courses of the summed posterior probability in the three maze sections.

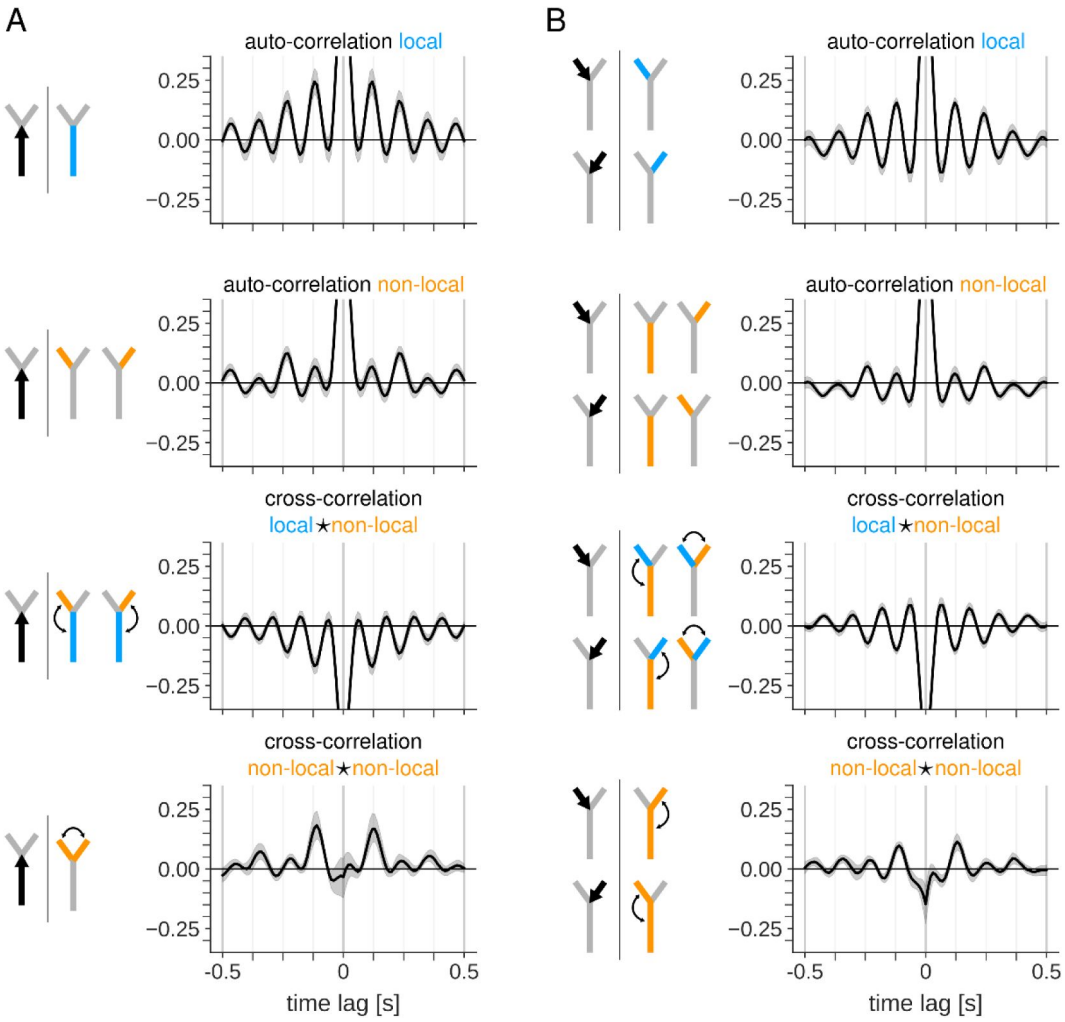

Figure 9.

Alternation of spatial representations on approach to choice point.

(A) Auto- and cross-correlation of posterior probability time courses for the three maze sections when the animal is running along the stem in the outbound direction towards the choice point. Correlations are computed as the Pearson correlation coefficient at varying time lags. For each plot, drawings at the left show the animal's behavior (black arrow) and the maze sections for which correlations are computed (color indicates whether the highlighted maze section is local (blue) or non-local (orange) relative to the animal's position on the track). Top: auto-correlation of local representations in the stem. Second from top: auto-correlations of non-local representations in the two goal arms. Third from top: cross-correlations between local and non-local representations. Bottom: cross-correlation between non-local representations in the two goal arms. (B) Same as (A), but for times when the animal is running along one of the goal arms in the inbound direction towards the choice point. Equivalent correlations for the two goal arms are computed jointly.

point) on either the stem (**Figure 9 - figure supplement 1A**) or goal arms (**Figure 9 - figure supplement 1B**).

Theta cycle skipping and alternation of spatial representations is more prominent in alternation task

We next asked if theta cycle skipping at the single cell level and theta time scale dynamics of spatial representations at the population level differed between the alternation task and the switching task. While in both tasks the animals visit left and right goal arms approximately equally during a session, the most highly rewarded goal arm changes from outbound journey to outbound journey in the alternation task, whereas it remains the same during a block of trials (until a switch) in the switching task. We split the recording sessions in two groups according to the behavioral task (n=6 for both tasks) and repeated the analysis of theta cycle skipping and temporal correlations of spatial representations.

We found that a higher fraction of cells showed evidence of theta cycle skipping in the spiking auto-correlogram during execution of the alternation task than the switching task (**Figure 10 - figure supplement 1**). The location on the maze where theta cycle skipping occurred differed between the two tasks. We observed stronger theta cycle skipping in the alternation task on approaches to the choice point in particular in the outbound direction (**Figure 10A,B**).

Finally, we analyzed the temporal dynamics of decoded spatial representations from the lateral septum cell population separately for the two behavioral tasks (**Figure 10C,D**). The cross-correlation of goal arm representations as animals approached the choice point in the outbound direction showed a higher peak at ~125ms in the alternation task than the switching task. This result indicates that the representations of the goal arms alternate more strongly ahead of the choice point when animals performed a task in which either goal arm potentially leads to reward.

Discussion

Our findings reveal that the lateral septum contains a population of neurons that alternatingly represents upcoming locations during adjacent theta cycles when rats approach a choice point. At the single cell level, this is supported by theta rhythmic spiking activity that is modulated at half theta frequency (i.e., theta cycle skipping). Our data shows that the alternating expression of spatial representations in the lateral septum is task dependent, which suggests that task demands and experience shape which representations are activated near a choice point. The lateral septum receives strong input from hippocampal place cells, and while there may be integration and transformation of incoming spatial signals, the theta-cycle dynamics of spatial representations appears to be transferred intact.

A majority of lateral septum cells in our dataset exhibited theta rhythmic spiking, which is generally consistent with previous reports (Bender et al., 2015; Pedemonte et al., 1998; Wirtshafter and Wilson, 2019). As we quantified rhythmicity from the spike train spectrum, it is possible that we missed low firing rate neurons that nonetheless have a theta-phase preference and thus we may have underestimated the percentage of theta-modulated neurons. Single cell properties differed between LSD and LSI, with cells in LSD exhibiting lower mean firing rates and stronger theta rhythmicity. Studies have indicated that the fraction of theta and power of theta rhythmic cells is more significant in the dorsal hippocampus (Royer et al., 2010; Schmidt et al., 2013). We now add that a similar dorsal-ventral gradient exists for theta cycle skipping.

Although the lateral septum receives strongly spatially modulated input from the hippocampus, reports on the percentage of cells in the lateral septum that convey spatial information in their firing rate vary considerably and range from 5% (Tingley and Buzsáki, 2018) to 56% (Wirtshafter

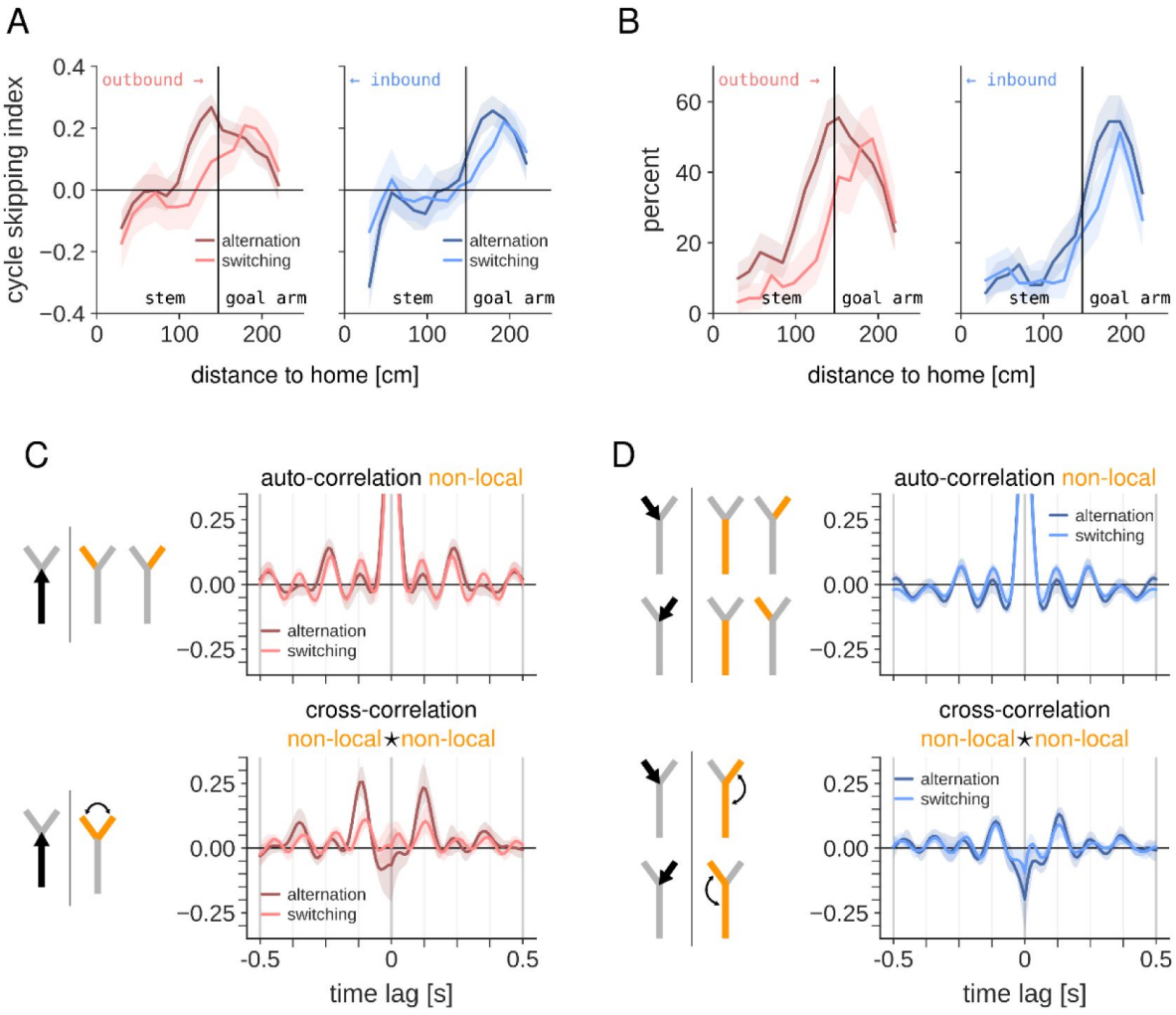

Figure 10.

Alternation of spatial representation is task dependent.

(A) Average CSI value as a function of location along outbound (left) and inbound (right) trajectories, separately for alternation and switching tasks. Shaded region represents 95% CI. (B) Same as (A) but for the percent of analyzed cells and trajectories with significant cycle skipping. (B) Auto- and cross-correlations of non-local spatial representations in the two goal arms as animals run outbound in the stem towards the choice point, computed separately for alternation and switching tasks. See **Figure 9** for details. (C) Same as (C), but for times when the animal is running along one of the goal arms in the inbound direction towards

and Wilson, 2019). The percentage of spatially modulated cells in our dataset sits at the upper end of this range. Some of this variation may be explained by the subregion that was sampled. Indeed, we find that a dorsal-ventral gradient in the percentage of spatially modulated cells, the amount of spatial information conveyed by single neurons, their preferred tuning for one of the goal arms and their directional selectivity (i.e. outbound vs inbound). The gradient mirrors the scaling of hippocampal place cell input along the dorsal-ventral axis. A second explanation for the high percentage of spatially modulated cells in our study could be the method used to identify these cells. We used a shuffling procedure that will identify also weakly modulated cells, whereas other studies have used a arbitrary cut-off of the spatial information metric, e.g. (Wirtshafter and Wilson, 2019). Even though the activity of a large fraction of lateral septum cells may be spatially modulated, the information content per spike is limited and comparable to what has been reported for the ventral hippocampus (Jung et al., 1994). Nevertheless, the population activity of lateral septum neurons contains sufficient spatial information for neural decoding of the animal's location and running direction on the maze with low error, conform (van der Veldt et al., 2021).

There is one notable property of hippocampal spatial coding that is absent in the lateral septum, namely the trajectory specific firing depending on the future path (prospective coding) or past path (retrospective coding) (Frank et al., 2000).

The single cell level analysis of temporal spiking patterns showed that theta cycle skipping occurred as animals approached the choice point as well as in the middle of the goal arms. The population decoding analysis, however, only pointed to alternating spatial representations of upcoming arms ahead of the choice point. It should be noted, however, that theta cycle skipping of single cells does not necessarily imply that two populations of neurons are activated in alternation. Likewise, cycle-by-cycle alternation of spatial representations at the population level can occur without observing theta cycle skipping in the spiking auto-correlation (e.g., when cells fire at a low rate). While the single cell and population analyses are consistent with each other as rats approach the choice point, it is currently not clear why an elevated theta cycle skipping is observed for individual cells in the goal arms. One explanation could be that a general reduction in excitatory drive and subsequently a drop in firing rate may result in the appearance of spiking at half-theta frequency. Alternatively, as our decoding analysis only looked at aggregate representations of the three maze arms, it is possible that alternating spatial representations are expressed at the population level but only of locations within a single arm.

Theta cycle skipping and alternating ensembles within adjacent theta cycles have been observed previously in the hippocampus (Kay et al., 2020), medial entorhinal cortex (Deshmukh et al., 2010), medial prefrontal cortex (Tang et al., 2021) and nucleus reuniens (Jankowski et al., 2014). Our result now extend this finding to the lateral septum and further point to the involvement of a large coordinated network. However, there are several notable similarities and differences between brain regions. In the hippocampus, representations of both future options appear to be expressed equally often ahead of the choice point (Kay et al., 2020; Tang et al., 2021). Our data indicates that the lateral septum behaves similarly, which is consistent with the strong direct projections from the hippocampus to the lateral septum. In contrast, while cells in the medial prefrontal cortex show strong theta cycle skipping, the corresponding theta spike sequences predicted the upcoming choice (Tang et al., 2021). Interestingly, theta cycle skipping has been observed in the nucleus reuniens, which links the medial prefrontal cortex and hippocampus (Griffin, 2015) and through this pathway mediates trajectory-dependent (prospective) activity in the hippocampus (Ito et al., 2015) and gates VTA dopaminergic activity (Zimmerman and Grace, 2016). However, given the differences between the theta cycle skipping properties of hippocampus and medial prefrontal cortex, the role of the nucleus reuniens needs further clarification. Finally, in the entorhinal cortex, theta cycle skipping has been preferentially linked to neurons that are tuned for head direction (Brandon et al., 2013), rather than place. The tendency for these head direction cells to skip alternate theta cycles increased from dorsal to

ventral entorhinal cortex, which is contrary to our observations in the lateral septum. The extent to which theta cycle skipping of head direction cells in the entorhinal cortex is functionally linked to theta cycle skipping in the hippocampal-lateral septum circuit is currently unknown and it is possible that they reflect distinct phenomena.

Individual theta cycles are often seen as a computational unit (Tang et al., 2021) that helps segregate spatial experiences or choices (Gupta et al., 2012; Jezek et al., 2011; Kay et al., 2020). When rats are exposed to an instant switch from one environment to another ("teleportation"), there is an transient flickering between preformed representations of the two environments (Jezek et al., 2011), which may be explained by two competing attractor states in the network. Similarly, the possible future paths at fork in the road may be represented by continuous attractors in the hippocampal network that compete with each other in each theta cycle. The alternation of these attractors from cycle to cycle suggest that the ensemble that was expressed in one theta cycle subsequently may be temporarily suppressed to favor the activation of another ensemble in the subsequent cycle. This may be seen as the system efficiently sampling the distribution of possible future trajectories using anti-correlated samples in subsequent theta cycles (Ujfalussy and Orbán, 2022). When there is reduced uncertainty about which future path to follow, e.g., in our switching task in which animals learn to follow one path to the high reward, the sampled distribution may be restricted to the one preferred path to reward, consistent with a reduction in theta cycle skipping and alternation of future path representations in the switching task. Further exploration is needed to understand how and on what timescale the samples are restricted in an experience or task-dependent manner.

Through the hippocampal-lateral septum pathway, the sampling of possible future paths could involve downstream hypothalamic and midbrain nuclei (Besnard and Leroy, 2022), including the ventral tegmental area (Luo et al., 2011). These brain regions may integrate motivational and reward value components with the sampled trajectories that could support tracking of the consequences of forthcoming actions on short time scales. If this is indeed the case, we predict that alternating representations of reward or other motivational signatures can be found in the projection areas of the lateral septum. Determining how the joint sampling of possible future trajectories and their outcomes contributes to learning processes in goal-oriented navigation and modulates decision-making will be an interesting direction for future studies.

Materials and methods

Experimental model and subject details

A total of 4 male Long Evans rats (280g to 350g) were used for this study. All experiments were carried out following protocols approved by the KU Leuven animal ethics committee (P119/2015 and P090/2021) in accordance with the European Council Directive (2016/63/EU). Each animal was familiarized to the experimenter for two weeks prior to the start of behavioral training. Following surgical implantation of neural probes, animals were housed separately in individually ventilated cages (IVC) with ad libitum access to water and controlled intake of food pellets. To motivate animals to run for reward in behavioral tasks, animals were food deprived to no less than 85% of their free feeding body weight. Body weight and general health status were checked daily by researchers and animal care personnel.

Behavioral training

Prior to surgery, animals were familiarized with a sleeping box and elevated linear track in the experimental room. On the linear track, animals were taught to shuttle back and forth between the two ends to collect reward (Choco-puffs). Next, animals were introduced to a Y-maze consisting of a 120 cm long stem and 76 cm long left/right choice arms. Animals were not pre-trained on the task, but only placed on the maze to initiate familiarization process and ease of training after the

surgical procedure. Once implanted, the animals were trained over several weeks in alternation and switching tasks. For the alternation task, each trial consisted of the outbound and inbound journey. On outbound journey animals had to choose one of the arms and if the choice was correct, they were rewarded with a Choco-puff. On the inbound journey, animals had to choose to go back to the starting position (correct choice) or they could go to the other arm. Animals could perform the task for a maximum of 30 minutes after which they were transported to the sleep box, where they rested for 30 minutes.

In the switching alternation task animals were placed only once on the maze (home location) and free to run on it. Animals had to learn to make a choice between left and right arm, the difference between the arms was the amount of reward given: 1 Choco-puff versus 5 Choco-puffs. After animals learned to only go to the higher rewarded arm, the valence was switched, and the opposite arm served now as the higher rewarded arm (measured as 8 consecutive visits). Animals had to learn the new rule. Each trial consisted of the outbound journey, where animals had to choose the arm and the inbound journey, where animals had to come back to the home location. Every new trial was initiated by an animal with a new outbound journey. Animals could perform the task for 45 minutes after which they were transported to the sleep box, where they rested for 30 minutes. The arm which contained the higher reward in the first trial was randomly chosen across 14 sessions using a sequence generator (*https://www.random.org/sequences/*).

Surgical procedure

Animals were implanted with a single-shank Neuropixels probe containing 960 electrodes and 384 read-out channels (imec, Leuven, Belgium; *https://ww.neuropixels.org*; (Jun et al., 2017)). The probe was mounted in a 3D printed fixture that enabled reuse of the probe (van Daal et al., 2021). Immediately prior to implantation, the probe shank was disinfected with 70% isopropyl alcohol and dip-coated with fluorescent dye DiI (ThermoFisher Scientific, USA). Surgeries were performed using standard aseptic techniques. Briefly, rats were anesthetized with isoflurane (induction: 4%, maintenance: 1-2%) and injected subcutaneously with the analgesic Metacam (5 mg/kg body weight; Boehringer Ingelheim Vetmedica GmbH). Throughout the surgery, breathing rate, heart rate and blood oxygen level were continuously monitored, and body temperature was kept constant with a rectal temperature sensor and heating pad (PhysioSuite, Kent Scientific, USA). After shaving the scalp with clippers, rats were carefully placed in a stereotaxic frame. Next, the scalp was disinfected with isobetadine and isopropyl alcohol and an incision was made along the midline to expose the skull. The skull was then scraped clean and dried before 7-8 anchoring bone screws (Fine Science Tools, Heidelberg, Germany) were gently screwed into small pre-drilled holes. One bone screw served as electrical ground. A craniotomy was made above the lateral septum at 0.3 mm anterior and 0.2 mm lateral relative to Bregma. After removal of the dura mater, the Neuropixels probe was inserted to a maximum depth of 7 mm at a 3° angle in the coronal plane using a motorized micromanipulator (for detailed implantation coordinates in each animal, see **Figure S1**). The implant was secured in place using meta-bond (C&B super bond, Brildent, India) and light-curable dental cement (SDI wave A2, Bayswater, Australia). Post-operative analgesic (subcutaneous injection of Metacam, 5mg/kg body weight) was administered once daily for three consecutive days.

Electrophysiological recordings

Electrophysiological data were collected using Neuropixels data acquisition hardware (imec, Leuven, Belgium) and SpikeGLX software (Bill Karsh, *https://github.com/billkarsh/SpikeGLX*). Position and head direction of the animal were tracked with an overhead video camera (50 Hz) using a Digilynx acquisition system and Cheetah software (Neuralynx, Bozeman, MT). In two animals (LS-k-7 and LS-k-8), two colored LEDs (red and blue) were mounted on the implant for tracking purposes. In the other animals, tracking was performed directly from the video images using DeepLabCut (Nath et al., 2019). Signals and video from the two acquisition systems were synchronized offline with the help of an external clock signal generated by an Arduino. The clock

signal consisted of regular pulses at 1 Hz with varying pulse durations. The clock signal was acquired on an extra analog channel of the Neuropixels hardware and a digital input channel of the Digilynx hardware. Offline synchronization was performed by determining the optimal alignment of the pulse durations in the two recorded clock signals.

Histology

Once the experiments were completed, animals were euthanized (Dolethal) and transcardially perfused with 4% formaldehyde following approved procedures. Brains were stored in 4% formaldehyde for 24h at 4°C after which they were transferred to 30% sucrose solution at 4°C until they were cut in 50 µm thick coronal slices with a cryostat (Leica, Germany). The brain slices were washed twice for 10 minutes with phosphate buffered saline (PBS), followed by staining with Neurotrace 500/525 green (1:300 for two hours, NeuroTrace™ 500/525 Green Fluorescent Nissl Stain - Solution in DMSO, Thermo Fisher Scientific, MA USA). Following two PBS washes, brain sections were additionally stained with DAPI (40, Diamidino-2-phenylindole dihydrochloride, Sigma-Aldrich, MA USA) for 30 minutes. Finally, brain slices were cover slipped with antifade medium (Vectashield, Vector, CA USA) and imaged on a confocal microscope (LSM 710, Zeiss, Germany) with a 10x objective.

Quantification and statistical analysis

Data analysis was carried out using Python and its scientific extension modules (Harris et al., 2020; McKinney, 2010; Virtanen et al., 2020), augmented with custom Python toolboxes.

Electrode locations in septal subregions

The location of the electrodes in the septal subregions was determined based on a combination of the probe implantation depth during surgery, the probe track in the histology and neural activity signatures, in particular the absence of neural activity in the white matter above the septal nuclei.

Spike sorting

Spikes were extracted and classified using Kilosort 3 (Pachitariu et al., 2016) followed by manual curation using the software Phy (*https://phy.readthedocs.io*).

Behavior

The behavior of the animals was separated into run trajectories that started and ended in one of the reward platforms at the end of the Y-maze arms. Run trajectories were categorized according to the arm of origin (e.g., left arm to stem or right arm) or according to the approach from/to the stem (outbound: from stem to left/right arm; inbound: from left/right arm to stem).

Theta modulation

To quantify the theta modulation of single cells, spike trains were binned at a resolution of 1 ms and a multi-taper power spectrum was computed for selected behavioral epochs (parameters for spectrum: window size = 2 s, bandwidth = 1 Hz).

To compute a theta modulation index, the power peak in the theta band (6-10 Hz) was detected and a frequency window (± 1.5 Hz) around the peak was defined. The base theta power is defined as the integrated power under the line that connects the power density at the start and end of the frequency window. The peak theta power is then defined as the integrated power above this line. Finally, the theta modulation index is computed as $\frac{peak-base}{peak+base}$. To determine if the theta modulation index was significantly higher than expected by chance, a shuffle distribution of modulation indices was computed for 500 locally time-jittered spike trains. For each spike, jitter was randomly

drawn from a gaussian distribution with standard deviation of half a theta cycle (62.5 ms). A theta modulation index was considered statistically significant if the Monte-Carlo p-value was smaller than 0.01.

Theta cycle skipping

The propensity of cells to increase their activity on alternating theta cycles was captured in a theta cycle skipping index that was calculated from the auto-correlogram (ACG) separately for each cell (Deshmukh et al., 2010; Kay et al., 2020). ACGs were computed from spikes in selected behavioral epochs, binned at 5 ms and smoothed with a gaussian window (bandwidth = 0.5 s). Cells with fewer than 50 spikes in the selected epochs were excluded from the analysis. In the ACG, the first and second theta-associated peak were detected: p_1, the peak in the 90-200 ms window nearest to 0 ms time lag, and p_2, the peak in the 200-400 ms window nearest to 0 ms time lag. For cases without peak p_1 or p_2, an ACG value was selected in lieu of the missing peak at half/double the time lag of the detected p_2/p_1 peak. The theta cycle skipping index was computed as $CSI = \frac{(p_2 - p_1)}{\max(p_1, p_2)}$.

To determine if a CSI value was higher than expected by chance, a shuffle distribution was computed from 250 locally randomized spike trains in which each spike was shifted by $k\theta$, with k randomly drawn from K = {−3, −2, −1,0,1,2,3} with probability $N(K_i)$ and θ = 125 ms. This spike randomization procedure was designed to destroy the cycle skipping structure but keep theta modulation intact. A CSI value was considered statistically significant if the Monte-Carlo p-value was smaller than 0.05.

As a measure of the time-varying instantaneous theta cycle skipping, we defined $CSI_i(t) = \frac{R_{[0.2,0.\bar{3}]}(t) - R_{[0.1,0.1\bar{6}]}(t)}{R_{[0.2,0.\bar{3}]}(t) + R_{[0.1,0.1\bar{6}]}(t)}$, where $R_{[L,U]}(t)$ represents the square root of the number of spike time pairs (s_i, s_j) surrounding t (i.e., $s_i < t$ and $s_j > t$) with an interval that lies within the [L,U] lag window (i.e., $L \le s_j - s_i \le U$). $R_{[L,U]}(t)$ was converted into a rate by normalizing to the lag window duration, evaluated at 10 ms time intervals and smoothed with a gaussian window (31.25 ms bandwidth). For time points with few surrounding spikes (i.e., $R_{[0.2,0.\bar{3}]}(t) + R_{[0.1,0.1\bar{6}]}(t) < \min(2, \frac{\mu}{2})$, where μ is the mean firing rate of the cell), $CSI_i(t)$ was set to zero. The value of $CSI_i(t)$ will be positive if spike pair intervals that fall in the theta skipping lag window (between 0.2 and $0.\bar{3}$ seconds) dominate over spike pair intervals in the theta lag window (between 0.1 and $0.1\bar{6}$ seconds).

Spatial tuning

The tracked animal position was converted to “linearized” location along the track by projecting the (x,y) coordinates to a skeletonized Y-maze. The position on the maze was defined as the distance from the home platform to (one of) the reward platform. For each cell, a spatial tuning curve $\lambda(x)$ in selected behavioral epochs was then constructed by computing compressed kernel density estimates (sampled at 1 cm resolution, gaussian kernel with bandwidth 10 cm; (Sodkomkham et al., 2016)) of spike counts and occupancy as a function of the linearized position.

To quantify spatial tuning, for each cell the spatial information was computed from the spatial tuning curve according to (Skaggs et al., 1992) and either expressed in bits/spike or bits/second. To test if the spatial information measure for a given cell was higher than expected by chance, a shuffle distribution was constructed from 250 randomized spike trains. For each randomization, spike times were circularly shifted by a random time offset only across the time epochs of interest. A cell was considered significantly spatially tuned if the Monte-Carlo p-value was less than 0.01.

Trajectory coding

To characterize trajectory specific coding for individual neurons, a selectivity index was computed as the normalized mean firing rate difference between two trajectories A and B: $SI_{AB} = \frac{|rate_A - rate_B|}{rate_A + rate_B}$.

For goal arm specific coding, a selectivity index was computed from the firing rates in the left and right goal arms separately for outbound ($SI_{goal|out}$) and inbound ($SI_{goal|in}$) journeys. For directional coding, a comparison was made between firing rates in the outbound and inbound journeys ($SI_{direction}$). To analyze prospective and retrospective coding, the firing rate on the stem of the Y-maze was compared between outbound journeys towards the left/right goal arms ($SI_{prospective}$) and inbound journeys starting from the left/right goal arms ($SI_{retrospective}$).

To determine if a selectivity index was higher than expected by chance, a shuffle distribution was constructed by randomly splitting the joint set of trajectories A and B into two new sets A' and B' and computing $SI_{A'B'}$ for 250 randomizations, under the null hypothesis that the firing rate is independent of trajectory. SI_{AB} was considered statistically significant if the Monte-Carlo p-value was smaller than 0.01.

Neural decoding

Bayesian neural decoding (Davidson et al., 2009; Zhang et al., 1998) was performed to estimate the position and running direction from the spiking activity of isolated lateral septum cells. Position on the track was "linearized" by concatenating the cumulative distances along the three sections of the maze (stem and left/right goal arms). Running direction was defined as a binary variable that represented movements in the inbound and outbound directions. For each cell, a tuning curve $\lambda(x, d)$ over linearized position and running direction was computed using compressed kernel density estimation (Sodkomkham et al., 2016) from all times when animals actively ran (speed > 10 cm/s) on stem and goal arms but excluding reward platforms. Given the presence of discontinuities in the linearized position, kernel densities were computed at discrete points on the track using a look-up table with precomputed distances between any two points that conform to the maze topology. For a time bin of duration Δ with $\boldsymbol{n} = [n_1, n_2, \ldots, n_{ncells}]$ spikes for all cells, the posterior probability over linearized position x and running direction d was computed assuming Poisson firing statistics and a non-informative prior:

$$P(x, d|\boldsymbol{n}) \propto \prod_{c=1}^{ncells} [\Delta\lambda_c(x, d)]^{n_c} e^{-\Delta\lambda_c(x,d)}$$

A K-fold cross-validation approach was used to evaluate the decoding performance, where K represents the total number of outbound and inbound journeys that an animal completed in a session. Thus, tuning curves were computed for all but one journey, and decoding was performed for the left-out journey in Δ = 200 ms time bins. This was repeated for all journeys. Posterior probability distributions were summarized by their maximum a posteriori point estimate and decoding performance was quantified as the median distance between estimated and true positions on the maze, and the percentage correct running direction estimates.

To evaluate the dependency of decoding performance on the number of cells included in the analysis, the cross-validated decoding approach was repeated for varying cell sample sizes. For each cell sample size, decoding performance was averaged across 25 different combinations of cells randomly drawn from all available cells. If the number of possible combinations was less than 25, then all combinations were used.

Neural decoding at theta time scale

For the analysis of spatial and directional representations at the time scale of theta oscillations, neural decoding was performed using the same encoding model as above that includes both LSD and LSI cells. Estimates were computed from spiking activity in Δ = 50 ms time bins with 80% overlap. To characterize the temporal dynamics of the decoded spatial estimates, signals were constructed that represent the summed posterior probability in each of the three maze arms. Auto- and cross-correlations were then computed of these signals separately for outbound and inbound trajectories to/from the left and right goals.

Acknowledgements

This work was supported by grants to F.K. from The Research Foundation – Flanders (FWO), grant numbers G0D7516N and G077321N.

Supplemental Figures

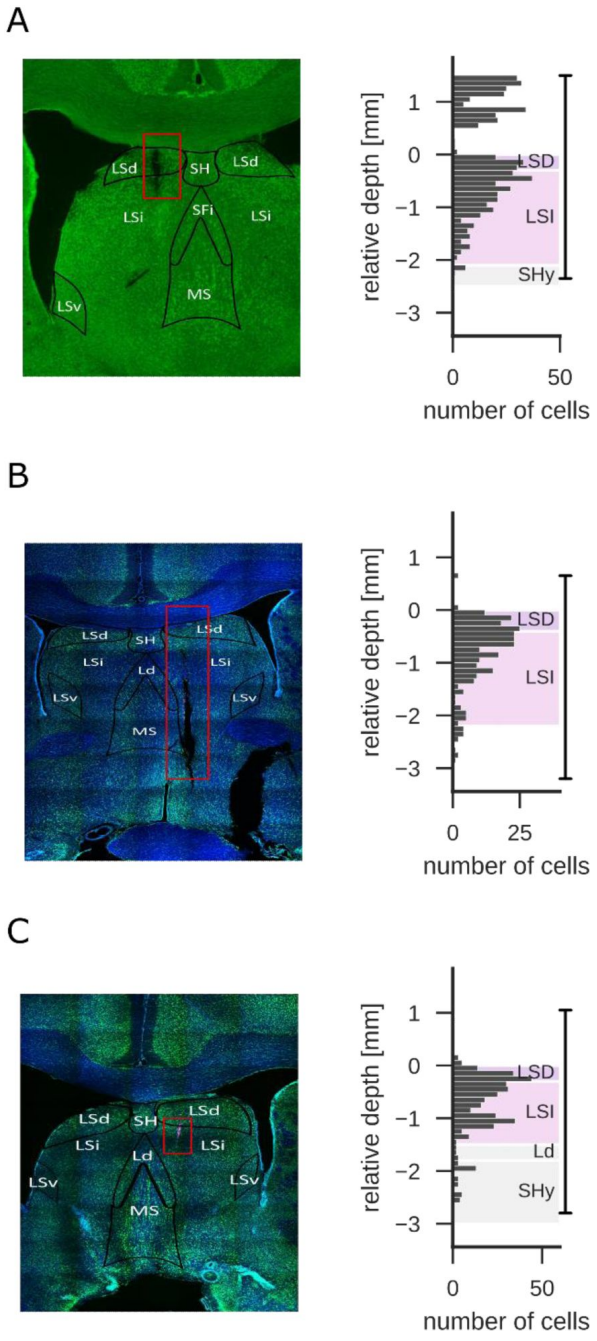

Figure 1 - figure supplement 1.

Left: coronal brain slice showing part of the Neuropixels probe trajectory (white arrow) in the lateral septum (animal, A: LS-k-8, B: LS-k-11, C: LS-k-14). Right: the number of recorded cells along the probe shank for one recording session in the same animal. Depth is measured relative to the white matter above the lateral septum. Vertical line at the right indicates the span of the recorded electrodes on the probe.

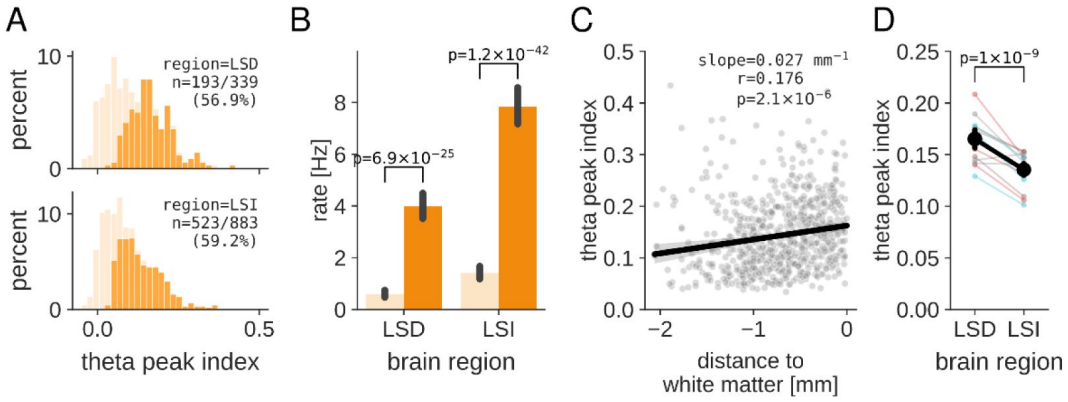

Figure 2 - figure supplement 1.

(A) Distribution of theta modulation index of all analyzed neurons in LSD and LSI. Light orange: full distribution of all cells. Dark orange: highlighted part of the distribution that represent cells with significant theta modulation index (Monte-Carlo p-value < 0.01). (B) Mean firing rate of theta rhythmic (dark orange) and non-rhythmic (light orange) cells differ significantly in both lateral septum subregions. Two-sided two-sample t-test, LSD: $t(337)=11.18$, $p=6.9\times10^{-25}$, LSI: $t(881)=14.45$, $p=1.2\times10^{-42}$. (C) Values of theta peak index for theta rhythmic cells increases for cells located closer to the white matter. Dots represent individual cells with significant theta peak index from all sessions and animals. Black line and shaded region represent linear fit and 95% confidence interval ($r=0.18$, $p=2.1\times10^{-6}$). (D) Mean value of theta peak index is significantly higher in LSD as compared to LSI (mean±sem theta peak index, LSD 0.17±0.005, LSI 0.13 ± 0.003; two-sided two-sample t-test, $t(714)=5.33$, $p=1.4\times10^{-7}$). Thin lines represent mean theta peak index for individual sessions, with the line color indicating the animal.

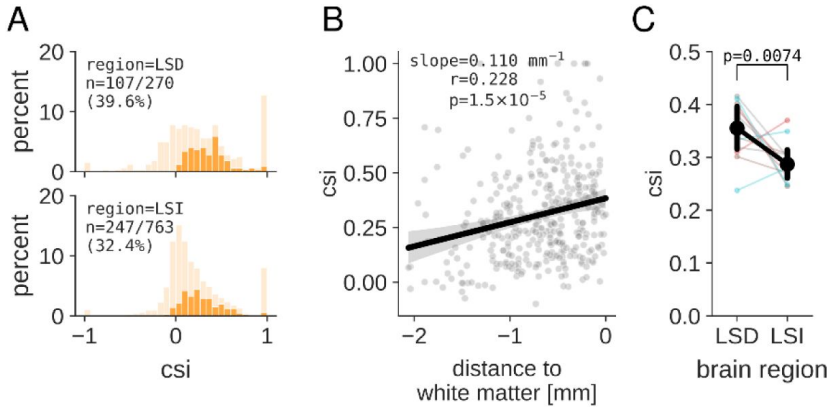

Figure 3 - figure supplement 1.

(A) Distribution of CSI values for all analyzed neurons in LSD and LSI. For each cell, the CSI value is taken from the trajectory with the highest z-scored CSI value relative to the shuffle distribution. Light orange: full distribution of all cells. Dark orange: highlighted part of the distribution that represent cells with significant CSI value (Monte-Carlo p-value < 0.05). (B) CSI values increase for cells located closer to the white matter. Dots represent individual cells with significant CSI value from all sessions and animals. For each cell, the CSI value is taken from the journey with the highest z-scored CSI value relative to the shuffle distribution. Black line and shaded region represent linear fit and 95% confidence interval ($r=0.23$, $p=1.5\times10^{-5}$). (C) Mean CSI value is significantly higher in LSD as compared to LSI (mean±sem CSI, LSD 0.36±0.02, LSI 0.29±0.01; two-sided two-sample t-test, $t(352)=2.70$, $p=0.0074$). Thin lines represent mean CSI value for individual sessions, with the line color indicating the animal.

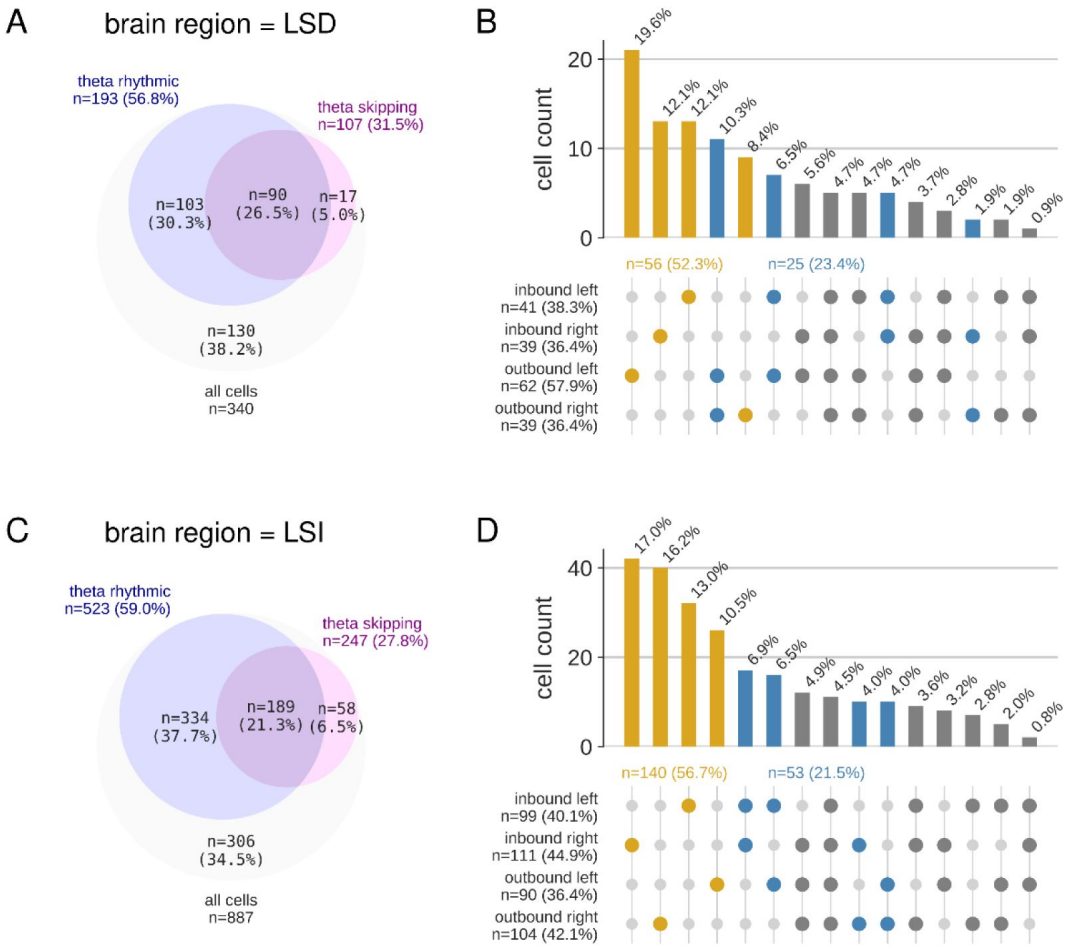

Figure 3 - figure supplement 2.

(A) Venn diagram showing overlap of cell populations with significant theta rhythmicity and theta cycle skipping in LSD (B) Histogram of the number of cells in LSD with a significant cycle skipping index for all possible journey combinations. Note that for most cells (52.3%; yellow) cycle skipping occurs only on a single journey type. For another population of cells (23.4%; blue), cycle skipping occurs on outbound, inbound, left, or right journeys. (C) Venn diagram showing overlap of cell populations with significant theta rhythmicity and theta cycle skipping in LSI (D) Histogram of the number of cells in LSI with a significant cycle skipping index for all possible journey combinations. Note that for most cells (56.7%; yellow) cycle skipping occurs only on a single journey type. For another population of cells (21.5%; blue), cycle skipping occurs on outbound, inbound, left, or right journeys.

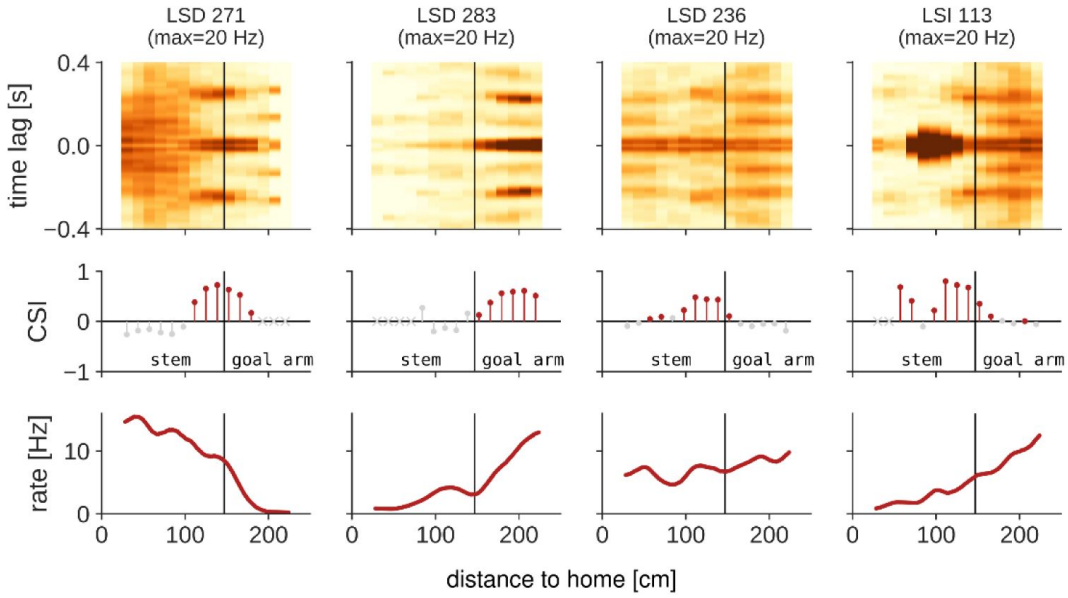

Figure 5 - figure supplement 1.

Spatially resolved auto-correlation (top), corresponding cycle skipping index (CSI; middle) and spatial tuning (bottom) for four example cells during outbound left journeys (animal LS-k-7). The same cells as in **Figure 4A** are shown). Auto-correlation and cycle skipping index were computed for overlapping 60 cm long sections along the trajectory to the goal. In the middle plot, colored points indicate significant cycle skipping ($p<0.05$), light grey crosses indicate that too few spikes (<50) were available and no cycle skipping index was computed. Black vertical lines indicate the choice point separating the stem and goal arms.

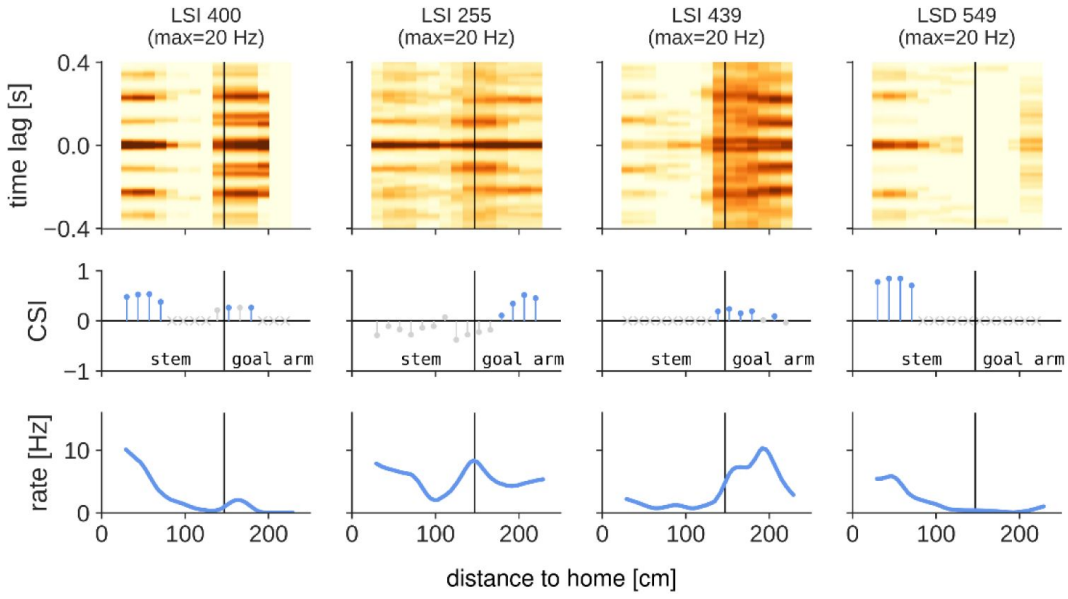

Figure 5 - figure supplement 2.

Spatially resolved auto-correlation (top), corresponding cycle skipping index (CSI; middle) and spatial tuning (bottom) for four example cells during inbound left journeys (animal LS-k-8). The same cells as in **Figure 4B** are shown. Auto-correlation and cycle skipping index were computed for overlapping 60 cm long sections along the trajectory to the goal. In the middle plot, colored points indicate significant cycle skipping ($p<0.05$), light grey crosses indicate that too few spikes (<50) were available and no cycle skipping index was computed. Black vertical lines indicate the choice point separating the stem and goal arms.

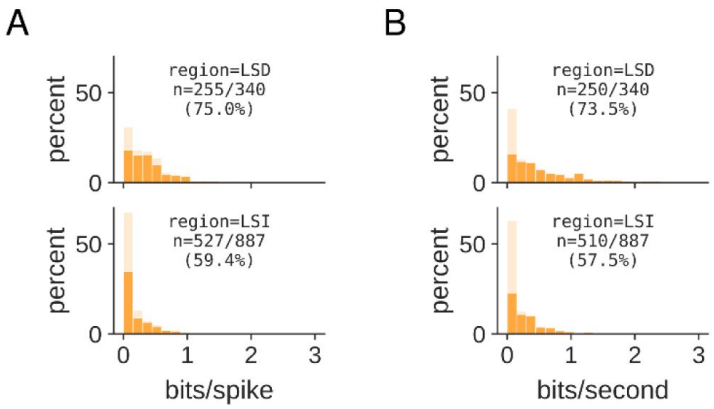

Figure 6 - figure supplement 1.

Distribution of spatial information in bits/spike (A) and bits/second (B) of all analyzed neurons in LSD (top) and LSI (bottom). Light orange: full distribution of all cells. Dark orange: highlighted part of the distribution that represent cells with significant spatial information (Monte-Carlo p-value < 0.01). Overall mean±sem spatial information in bits/spike: LSD 0.42±0.02, LSI 0.21±0.01.

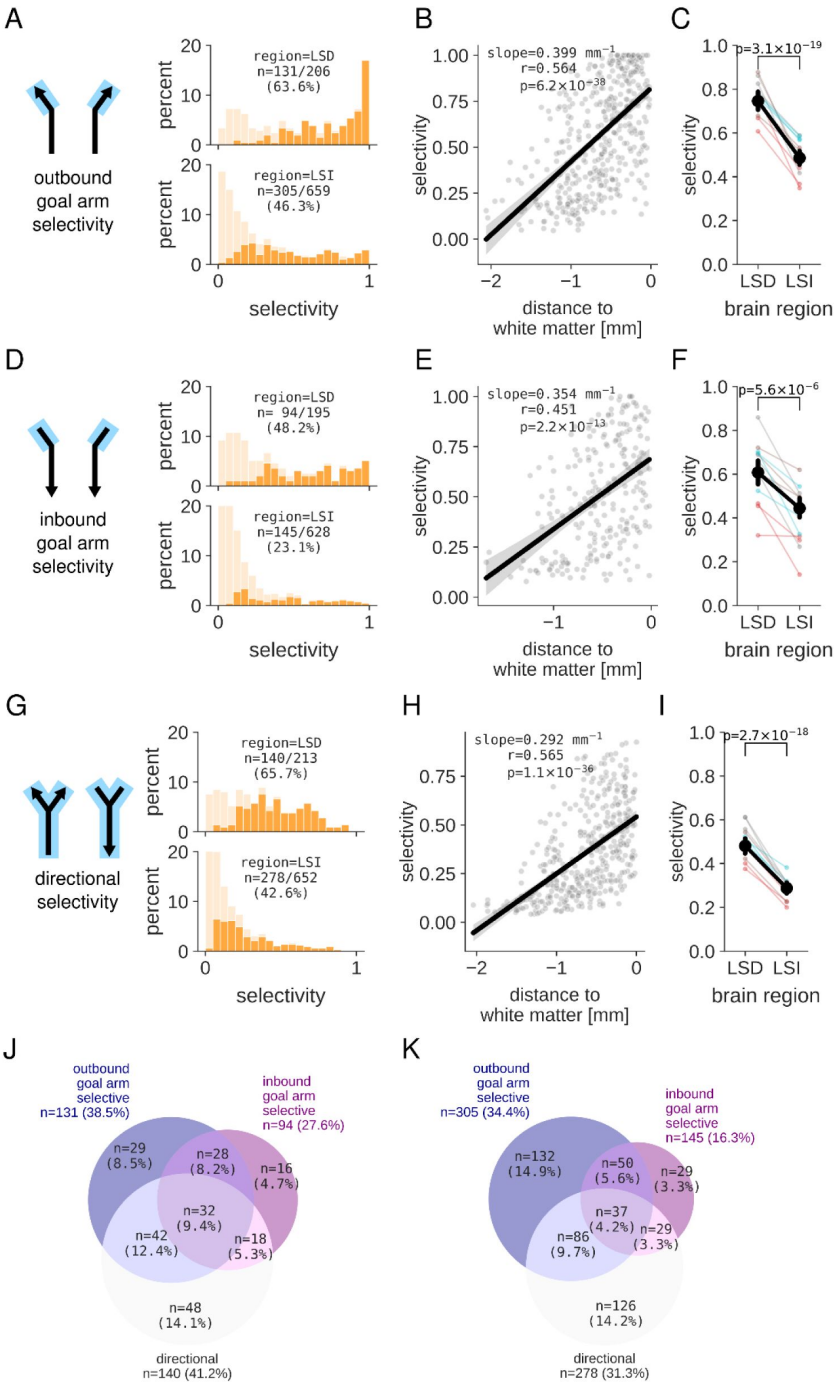

Figure 6 - figure supplement 2.

(A,B,C) Distribution of outbound goal arm (A), inbound goal arm (B) and directional (C) selectivity of all analyzed neurons in LSD and LSI. Light orange: full distribution of all cells. Dark orange: highlighted part of the distribution that represent cells with significant selectivity (Monte-Carlo p-value < 0.01). (D,E,F) Values of outbound goal arm (D), inbound goal arm (E) and directional (F) selectivity index increases for cells located closer to the white matter. Dots represent individual cells with significant selectivity index from all sessions and animals. Black line and shaded region represent linear fit and 95% confidence interval. (G,H,I) Mean value of outbound goal arm (G), inbound goal arm (H) and directional (I) selectivity index is significantly higher in LSD as compared to LSI (mean±sem selectivity, outbound goal arm: LSD 0.75±0.02, LSI 0.49±0.02, two-sided two-sample t-test, $t(434)=9.40$, $p=3.1\times10^{-19}$; inbound goal arm: LSD 0.61±0.03, LSI 0.44±0.02, two-sided two-sample t-test, $t(237)=4.65$, $p=5.6\times10^{-6}$; directional: LSD 0.48±0.02, LSI 0.29±0.01, two-sided two-sample t-test, $t(416)=9.14$, $p=2.7\times10^{-18}$). (J,K) Overlap between goal arm and directional selectivity for cells

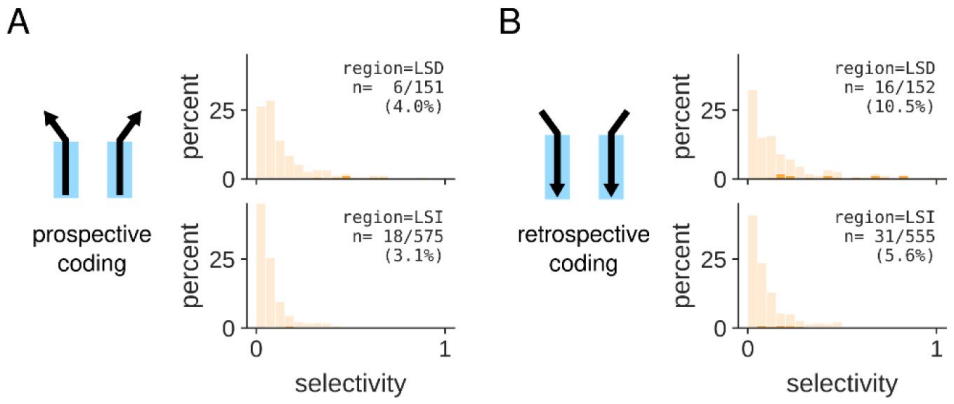

Figure 6 - figure supplement 3.

(A) Distribution of prospective coding of all analyzed neurons in LSD and LSI. Light orange: full distribution of all cells. Dark orange: highlighted part of the distribution that represent cells with significant prospective coding (Monte-Carlo p-value < 0.01). (B) Distribution of retrospective coding of all analyzed neurons in LSD and LSI. Light orange: full distribution of all cells. Dark orange: highlighted part of the distribution that represent cells with significant retrospective coding (Monte-Carlo p-value < 0.01).

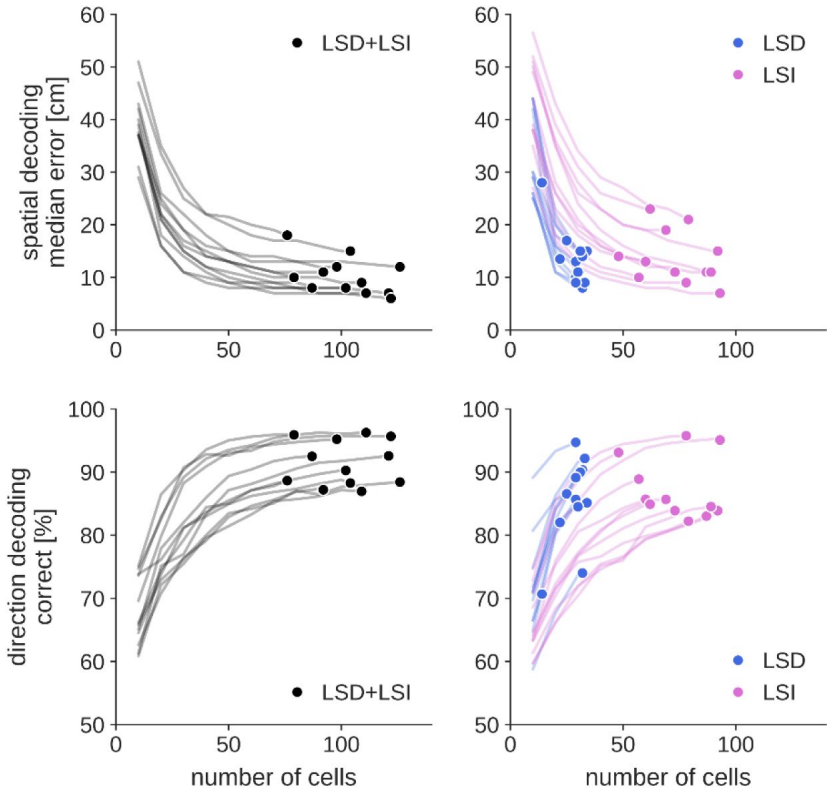

Figure 7 - figure supplement 1.

Dependency of decoding performance for position (top) and direction (bottom) on the number cells included in the analysis. Left: all LSD and LSI combined; right: separately for LSD and LSI cells. The result for each session is plotted separately. Dots: the decoding performance for each session when including all available cells. Lines: the decoding performance for each session when subsampling the cells. Note that for a similar decoding performance, fewer LSD cells than LSI are required.

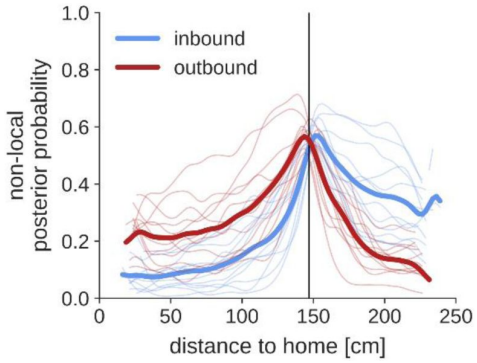

Figure 8 - figure supplement 1.

Average posterior probability following theta time scale decoding that is assigned to non-local maze arms (i.e., the arms where the animal is not currently located). Data for the goal arms is combined and position is expressed as distance to home. Vertical line indicates the choice point. Thin lines represent data for individual sessions; thick lines represent average across sessions.

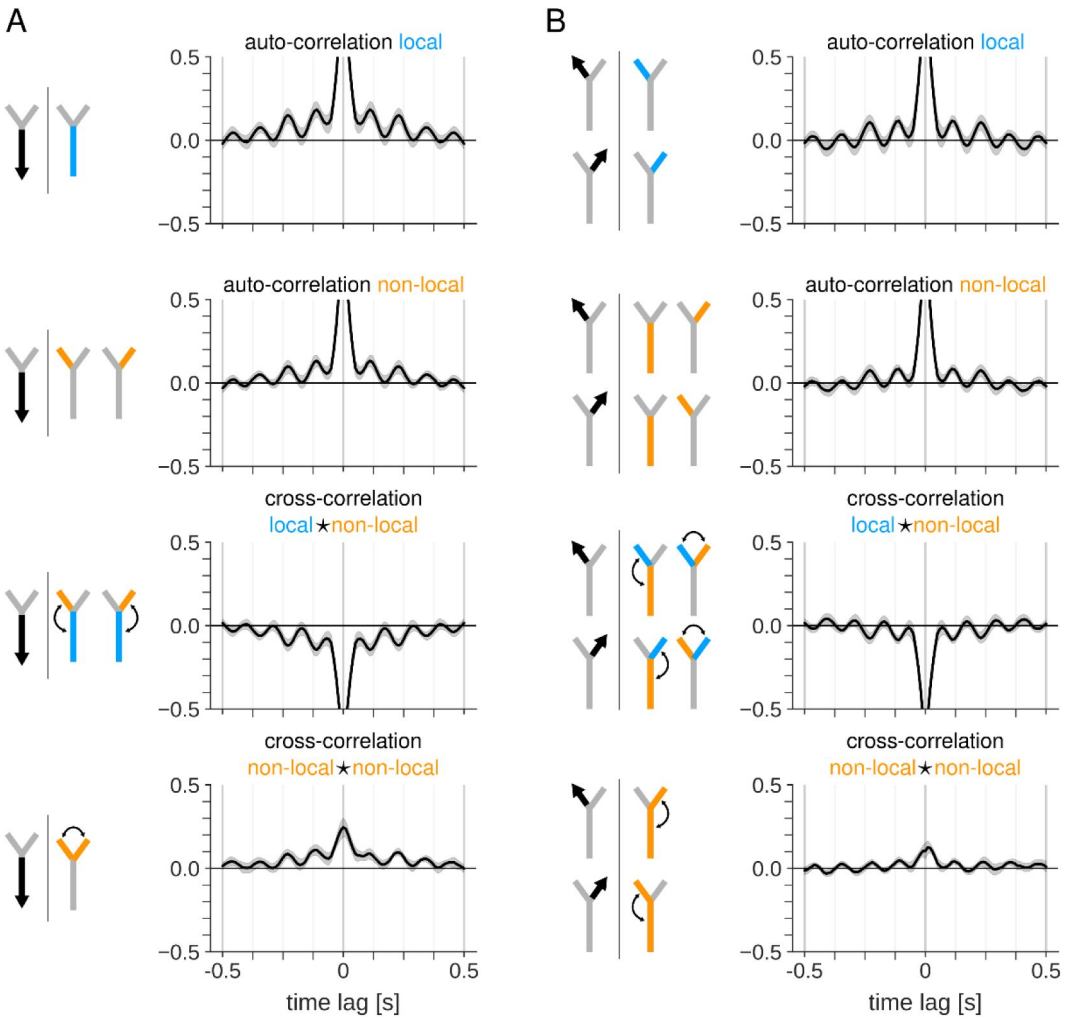

Figure 9 - figure supplement 1.

(A) Auto- and cross-correlation of posterior probability time courses for the three maze sections when the animal is running along the stem in the inbound direction towards home. Correlations are computed as the Pearson correlation coefficient at varying time lags. For each plot, drawings at the left show the animal's behavior (black arrow) and the maze sections for which correlations are computed (color indicates whether the highlighted maze section is local (blue) or non-local (orange) relative to the animal's position on the track). Top: auto-correlation of local representations in the stem. Second from top: auto-correlations of non-local representations in the two goal arms. Third from top: cross-correlations between local and non-local representations. Bottom: cross-correlation between non-local representations in the two goal arms. (B) Same as (A), but for times when the animal is running along one of the goal arms in the outbound direction towards the reward platform. Equivalent correlations for the two goal arms are computed jointly.

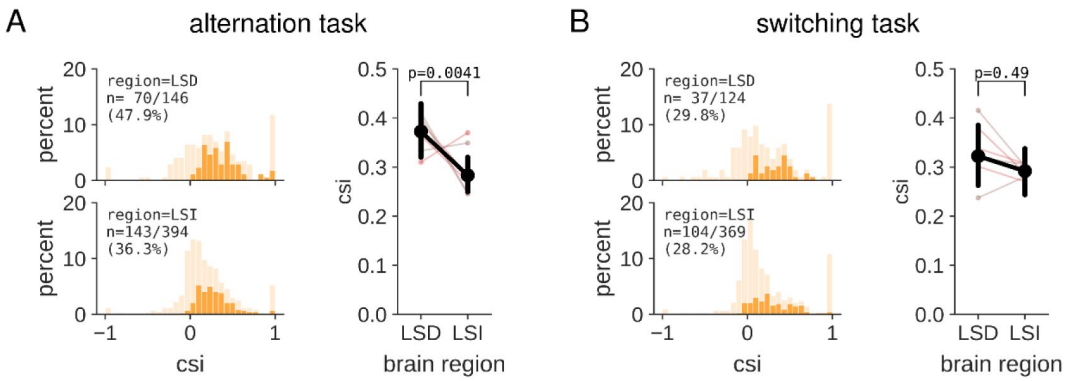

Figure 10 - figure supplement 1.

(A) Left: distribution of CSI values for LSD (top) and LSI (bottom) neurons in sessions in which rats performed the alternation task. For each cell, the CSI value is taken from the trajectory with the highest z-scored CSI value relative to the shuffle distribution. Light orange: full distribution of all cells. Dark orange: highlighted part of the distribution that represent cells with significant CSI value (Monte-Carlo p-value < 0.05). Right: mean CSI value is significantly higher in LSD as compared to LSI (mean±sem CSI, LSD 0.37±0.03, LSI 0.28±0.02; two-sided two-sample t-test, t(211)=2.90, p=0.0041). Thin lines represent mean CSI value for individual sessions, with the line color indicating the animal. (B) Same as (A), but for sessions in which animals performed the switching task. Mean CSI value (right) is not different between LSD and LSI (mean±sem CSI, LSD 0.32±0.03, LSI 0.29±0.02; two-sided two-sample t-test, t(139)=0.69, p=0.49).

References

Bender F, Gorbati M, Cadavieco MC, Denisova N, Gao X, Holman C, Korotkova T, Ponomarenko A (2015) **Theta oscillations regulate the speed of locomotion via a hippocampus to lateral septum pathway** *Nat Commun* **6** https://doi.org/10.1038/ncomms9521

Besnard A, Leroy F (2022) **Top-down regulation of motivated behaviors via lateral septum sub-circuits** *Mol Psychiatry* **27**:3119–3128 https://doi.org/10.1038/s41380-022-01599-3

Brandon MP, Bogaard AR, Schultheiss NW, Hasselmo ME (2013) **Segregation of cortical head direction cell assemblies on alternating θ cycles** *Nat Neurosci* **16**:739–48 https://doi.org/10.1038/nn.3383

Colgin LL (2013) **Mechanisms and functions of theta rhythms** *Annu Rev Neurosci* **36**:295–312 https://doi.org/10.1146/annurev-neuro-062012-170330

Davidson TJ, Kloosterman F, Wilson M a (2009) **Hippocampal replay of extended experience** *Neuron* **63**:497–507 https://doi.org/10.1016/j.neuron.2009.07.027

Deshmukh SS, Yoganarasimha D, Voicu H, Knierim JJ (2010) **Theta modulation in the medial and the lateral entorhinal cortices** *J Neurophysiol* **104**:994–1006 https://doi.org/10.1152/jn.01141.2009

Frank LM, Brown EN, Wilson M (2000) **Trajectory encoding in the hippocampus and entorhinal cortex** *Neuron* **27**:169–78 https://doi.org/10.1016/s0896-6273(00)00018-0

Griffin AL (2015) **Role of the thalamic nucleus reuniens in mediating interactions between the hippocampus and medial prefrontal cortex during spatial working memory** *Front Syst Neurosci* **9** https://doi.org/10.3389/fnsys.2015.00029

Gupta AS, van der Meer MAA, Touretzky DS, Redish AD. (2012) **Segmentation of spatial experience by hippocampal θ sequences** *Nat Neurosci* **15**:1032–9 https://doi.org/10.1038/nn.3138

Harris CR, Millman KJ, van der Walt SJ, Gommers R, Virtanen P, Cournapeau D, Wieser E, Taylor J, Berg S, Smith NJ, Kern R, Picus M, Hoyer S, van Kerkwijk MH, Brett M, Haldane A, del Río JF, Wiebe M, Peterson P, Gérard-Marchant P, Sheppard K, Reddy T, Weckesser W, Abbasi H, Gohlke C, Oliphant TE (2020) **Array programming with NumPy** *Nature* **585**:357–362 https://doi.org/10.1038/s41586-020-2649-2

Ito HT, Zhang S-J, Witter MP, Moser EI, Moser M-B (2015) **A prefrontal-thalamo-hippocampal circuit for goal-directed spatial navigation** *Nature* **522**:50–5 https://doi.org/10.1038/nature14396

Jankowski MM, Islam MN, Wright NF, Vann SD, Erichsen JT, Aggleton JP, O'Mara SM (2014) **Nucleus reuniens of the thalamus contains head direction cells** *Elife* **3** https://doi.org/10.7554/eLife.03075

Jezek K, Henriksen EJ, Treves A, Moser EI, Moser M-B (2011) **Theta-paced flickering between place-cell maps in the hippocampus** *Nature* **478**:246–9 https://doi.org/10.1038/nature10439

Jun JJ, Steinmetz NA, Siegle JH, Denman DJ, Bauza M, Barbarits B, Lee AK, Anastassiou CA, Andrei A, Aydın Ç, Barbic M, Blanche TJ, Bonin V, Couto J, Dutta B, Gratiy SL, Gutnisky DA, Häusser M, Karsh B, Ledochowitsch P, Lopez CM, Mitelut C, Musa S, Okun M, Pachitariu M, Putzeys J, Rich PD, Rossant C, Sun W-L, Svoboda K, Carandini M, Harris KD, Koch C, O'Keefe J, Harris TD (2017) **Fully integrated silicon probes for high-density recording of neural activity** *Nature* **551**:232–236 https://doi.org/10.1038/nature24636

Jung MW, Wiener SI, McNaughton BL (1994) **Comparison of spatial firing characteristics of units in dorsal and ventral hippocampus of the rat** *J Neurosci* **14**:7347–56 https://doi.org/10.1523/JNEUROSCI.14-12-07347.1994

Kay K, Chung JE, Sosa M, Schor JS, Karlsson MP, Larkin MC, Liu DF, Frank LM (2020) **Constant Sub-second Cycling between Representations of Possible Futures in the Hippocampus** *Cell* **180**:552–567 https://doi.org/10.1016/j.cell.2020.01.014

Leutgeb S, Mizumori SJY (2002) **Context-specific spatial representations by lateral septal cells** *Neuroscience* **112**:655–63 https://doi.org/10.1016/s0306-4522(02)00101-x

Luo AH, Tahsili-Fahadan P, Wise RA, Lupica CR, Aston-Jones G (2011) **Linking Context with Reward: A Functional Circuit from Hippocampal CA3 to Ventral Tegmental Area** *Science (1979)* **333**:353–357 https://doi.org/10.1126/science.1204622

McKinney W (2010) **Data Structures for Statistical Computing in PythonProceeding of the 9th Python in Science Conference** :56–61 https://doi.org/10.25080/Majora-92bf1922-00a

Monmaur P, Ayadi K, Breton P (1993) **Hippocampal EEG responses induced by carbachol and atropine infusions into the septum and the hippocampus in the urethane-anaesthetized rat** *Brain Res* **631**:317–24 https://doi.org/10.1016/0006-8993(93)91551-3

Nath T, Mathis A, Chen AC, Patel A, Bethge M, Mathis MW (2019) **Using DeepLabCut for 3D markerless pose estimation across species and behaviors** *Nat Protoc* **14**:2152–2176 https://doi.org/10.1038/s41596-019-0176-0

Opalka AN, Wang D V (2020) **Hippocampal efferents to retrosplenial cortex and lateral septum are required for memory acquisition** *Learn Mem* **27**:310–318 https://doi.org/10.1101/lm.051797.120

Pachitariu M, Steinmetz N, Kadir S, Carandini M, Harris K (2016) **Fast and accurate spike sorting of high-channel count probes with KiloSort** *Adv Neural Inf Process Syst* :4455–4463

Pedemonte M, Barrenechea C, Nuñez A, Gambini JP, García-Austt E (1998) **Membrane and circuit properties of lateral septum neurons: relationships with hippocampal rhythms** *Brain Res* **800**:145–53 https://doi.org/10.1016/s0006-8993(98)00517-4

Rizzi-Wise CA, Wang D V (2021) **Putting Together Pieces of the Lateral Septum: Multifaceted Functions and Its Neural Pathways** *eNeuro* **8** https://doi.org/10.1523/ENEURO.0315-21.2021

Robinson JC, Brandon MP (2021) **Skipping ahead: A circuit for representing the past, present, and future** *Elife* **10** https://doi.org/10.7554/eLife.68795

Royer S, Sirota A, Patel J, Buzsáki G (2010) **Distinct representations and theta dynamics in dorsal and ventral hippocampus** *J Neurosci* **30**:1777–87 https://doi.org/10.1523/JNEUROSCI.4681-09.2010

Schmidt B, Hinman JR, Jacobson TK, Szkudlarek E, Argraves M, Escabí MA, Markus EJ (2013) **Dissociation between dorsal and ventral hippocampal theta oscillations during decision-making** *J Neurosci* **33**:6212–24 https://doi.org/10.1523/JNEUROSCI.2915-12.2013

Skaggs WE, McNaughton BL, Gothard KM, Markus EJ. (1992) **An information-theoretic approach to deciphering the hippocampal code** :1039–1037

Sodkomkham D, Ciliberti D, Wilson MA, Fukui K-I, Moriyama K, Numao M, Kloosterman F (2016) **Kernel density compression for real-time Bayesian encoding/decoding of unsorted hippocampal spikes** *Knowl Based Syst* **94**:1–12 https://doi.org/10.1016/j.knosys.2015.09.013

Tang W, Shin JD, Jadhav SP (2021) **Multiple time-scales of decision-making in the hippocampus and prefrontal cortex** *Elife* **10** https://doi.org/10.7554/eLife.66227

Tingley D, Buzsáki G (2018) **Transformation of a Spatial Map across the Hippocampal-Lateral Septal Circuit** *Neuron* **98**:1229–1242 https://doi.org/10.1016/j.neuron.2018.04.028

Trent NL, Menard JL (2010) **The ventral hippocampus and the lateral septum work in tandem to regulate rats' open-arm exploration in the elevated plus-maze** *Physiol Behav* **101**:141–52 https://doi.org/10.1016/j.physbeh.2010.04.035

Ujfalussy BB, Orbán G (2022) **Sampling motion trajectories during hippocampal theta sequences** *Elife* **11** https://doi.org/10.7554/eLife.74058

van Daal RJJ, Aydin Ç, Michon F, Aarts AAA, Kraft M, Kloosterman F, Haesler S. (2021) **Implantation of Neuropixels probes for chronic recording of neuronal activity in freely behaving mice and rats** *Nat Protoc* **16**:3322–3347 https://doi.org/10.1038/s41596-021-00539-9

van der Veldt S, Etter G, Mosser C-A, Manseau F, Williams S. (2021) **Conjunctive spatial and self-motion codes are topographically organized in the GABAergic cells of the lateral septum** *PLoS Biol* **19** https://doi.org/10.1371/journal.pbio.3001383

Virtanen P, Gommers R, Oliphant TE, Haberland M, Reddy T, Cournapeau D, Burovski E, Peterson P, Weckesser W, Bright J, van der Walt SJ, Brett M, Wilson J, Millman KJ, Mayorov N, Nelson ARJ, Jones E, Kern R, Larson E, Carey CJ, Polat İ, Feng Y, Moore EW, VanderPlas J, Laxalde D, Perktold J, Cimrman R, Henriksen I, Quintero EA, Harris CR, Archibald AM, Ribeiro AH, Pedregosa F, van Mulbregt P (2020) **SciPy 1.0: fundamental algorithms for scientific computing in Python** *Nat Methods* https://doi.org/10.1038/s41592-019-0686-2

Wirtshafter HS, Wilson MA (2021) **Lateral septum as a nexus for mood, motivation, and movement** *Neurosci Biobehav Rev* **126**:544–559 https://doi.org/10.1016/j.neubiorev.2021.03.029

Wirtshafter HS, Wilson MA (2020) **Differences in reward biased spatial representations in the lateral septum and hippocampus** *Elife* **9** https://doi.org/10.7554/eLife.55252

Wirtshafter HS, Wilson MA (2019) **Locomotor and Hippocampal Processing Converge in the Lateral Septum** *Curr Biol* **29**:3177–3192 https://doi.org/10.1016/j.cub.2019.07.089

Zhang K, Ginzburg I, McNaughton BL, Sejnowski TJ (1998) **Interpreting neuronal population activity by reconstruction: unified framework with application to hippocampal place cells** *J Neurophysiol* **79**:1017–44

Zhou TL, Tamura R, Kuriwaki J, Ono T (1999) **Comparison of medial and lateral septal neuron activity during performance of spatial tasks in rats** *Hippocampus* **9**:220–34 https://doi.org/10.1002/(SICI)1098-1063(1999)9:3<220::AID-HIPO3>3.0.CO;2-E

Zimmerman EC, Grace AA (2016) **The Nucleus Reuniens of the Midline Thalamus Gates Prefrontal-Hippocampal Modulation of Ventral Tegmental Area Dopamine Neuron Activity** *J Neurosci* **36**:8977–84 https://doi.org/10.1523/JNEUROSCI.1402-16.2016

Article and author information

Katarzyna Bzymek
Brain & Cognition, KU Leuven, Leuven, Belgium, Neuro-Electronics Research Flanders, Leuven, Belgium

Fabian Kloosterman
Brain & Cognition, KU Leuven, Leuven, Belgium, Neuro-Electronics Research Flanders, Leuven, Belgium, Lead Contact
For correspondence: kloosterman.fabian@gmail.com
ORCID iD: 0000-0001-6680-9660

Copyright

Editors

Reviewing Editor
Emilio Kropff
Leloir Institute - IIBBA/CONICET, Argentina

Senior Editor
Laura Colgin
University of Texas at Austin, United States of America

Reviewer #1 (Public Review):

Summary:
The authors provide very compelling evidence that the lateral septum (LS) engages in theta cycle skipping.

Strengths:
The data and analysis are highly compelling regarding the existence of cycle skipping.

Weaknesses:
The manuscript falls short on describing the behavioral or physiological importance of the witnessed theta cycle skipping, and there is a lack of attention to detail with some of the findings and figures:

More/any description is needed in the article text to explain the switching task and the behavioral paradigm generally. This should be moved from only being in methods as it is essential for understanding the study.

An explanation is needed as to how a cell can be theta skipping if it is not theta rhythmic.

The most interesting result, in my opinion, is the last paragraph of the entire results section, where there is more switching in the alternation task, but the reader is kind of left hanging as to how this relates to other findings. How does this relate to differences in decoding of relative arms (the correct or incorrect arm) during those theta cycles or to the animal's actual choice? Similarly, how does it relate to the animal's actual choice? Is this phenomenon actually behaviorally or physiologically meaningful at all? Does it contribute at all to any sort of planning or decision-making?

The authors state that there is more cycle skipping in the alternation task than in the switching task, and that this switching occurs in the lead-up to the choice point. Then they say there is a higher peak at ~125 in the alternation task, which is consistent. However, in the final sentence, the authors note that "This result indicates that the representations of the goal arms alternate more strongly ahead of the choice point when animals performed a task in which either goal arm potentially leads to reward." Doesn't either arm potentially lead to a reward (but different amounts) in the switching task, not the alternation task? Yet switching is stronger in the alternation task, which is not constant and contradicts this last sentence.

Additionally, regarding the same sentence - "representations of the goal arms alternate more strongly ahead of the choice point when the animals performed a task in which either goal arm potentially leads to reward." - is this actually what is going on? Is there any reason at all to think this has anything to do with reward versus just a navigational choice?

Similarly, the authors mention several times that the LS links the HPC to 'reward' regions in the brain, and it has been found that the LS represents rewarded locations comparatively more than the hippocampus. How does this relate to their finding?

Reviewer #2 (Public Review):

Summary
Recent evidence indicates that cells of the navigation system representing different directions and whole spatial routes fire in a rhythmic alternation during 5-10 Hz (theta) network oscillation (Brandon et al., 2013, Kay et al., 2020). This phenomenon of theta cycle skipping was also reported in broader circuitry connecting the navigation system with the cognitive control regions (Jankowski et al., 2014, Tang et al., 2021). Yet nothing was known about the translation of these temporally separate representations to midbrain regions involved in reward processing as well as the hypothalamic regions, which integrate metabolic, visceral, and sensory signals with the descending signals from the forebrain to ensure adaptive control of innate behaviors (Carus-Cadavieco et al., 2017). The present work aimed to investigate theta cycle skipping and alternating representations of trajectories in the lateral septum, neurons of which receive inputs from a large number of CA1 and nearly all CA3 pyramidal cells (Risold and Swanson, 1995). While spatial firing has been reported in the lateral septum before (Leutgeb and Mizumori, 2002, Wirtshafter and Wilson, 2019), its dynamic aspects have remained elusive. The present study replicates the previous findings of theta-rhythmic neuronal activity in the lateral septum and reports a temporal alternation of spatial representations in this region, thus filling an important knowledge gap and significantly extending the understanding of the processing of spatial information in the brain. The lateral septum thus propagates the representations of alternative spatial behaviors to its efferent regions. The results can instruct further research of neural mechanisms

supporting learning during goal-oriented navigation and decision-making in the behaviourally crucial circuits entailing the lateral septum.

Strengths
To this end, cutting-edge approaches for high-density monitoring of neuronal activity in freely behaving rodents and neural decoding were applied. Strengths of this work include comparisons of different anatomically and probably functionally distinct compartments of the lateral septum, innervated by different hippocampal domains and projecting to different parts of the hypothalamus; large neuronal datasets including many sessions with simultaneously recorded neurons; consequently, the rhythmic aspects of the spatial code could be directly revealed from the analysis of multiple spike trains, which were also used for decoding of spatial trajectories; and comparisons of the spatial coding between the two differently reinforced tasks.

Weaknesses
Possible in principle, with the present data across sessions, longitudinal analysis of the spatial coding during learning the task was not performed. Without using perturbation techniques, the present approach could not identify the aspects of the spatial code actually influencing the generation of behaviors by downstream regions.

Reviewer #3 (Public Review):

Summary:
Bzymek and Kloosterman carried out a complex experiment to determine the temporal spike dynamics of cells in the dorsal and intermediate lateral septum during the performance of a Y-maze spatial task. In this descriptive study, the authors aim to determine if inputting spatial and temporal dynamics of hippocampal cells carry over to the lateral septum, thereby presenting the possibility that this information could then be conveyed to other interconnected subcortical circuits. The authors are successful in these aims, demonstrating that the phenomenon of theta cycle skipping is present in cells of the lateral septum. This finding is a significant contribution to the field as it indicates the phenomenon is present in neocortex, hippocampus, and the subcortical hub of the lateral septal circuit. In effect, this discovery closes the circuit loop on theta cycle skipping between the interconnected regions of the entorhinal cortex, hippocampus, and lateral septum. Moreover, the authors make 2 additional findings: 1) There are differences in the degree of theta modulation and theta cycle skipping as a function of depth, between the dorsal and intermediate lateral septum; and 2) The significant proportion of lateral septum cells that exhibit theta cycle skipping, predominantly do so during 'non-local' spatial processing.

Strengths: The major strength of the study lies in its design, with 2 behavioral tasks within the Y-maze and a battery of established analyses drawn from prior studies that have established spatial and temporal firing patterns of entorhinal and hippocampal cells during these tasks. Primary among these analyses, is the ability to decode the animal's position relative to locations of increased spatial cognitive demand, such as the choice point before the goal arms. The presence of theta cycle skipping cells in the lateral septum is robust and has significant implications for the ability to dissect the generation and transfer of spatial routes to goals within and between the neocortex and subcortical neural circuits.

Weaknesses: There are no major discernable weaknesses in the study, yet the scope and mechanism of the theta cycle phenomenon remain to be placed in the context of other phenomena indicative of spatial processing independent of the animal's current position. An example of this would be the ensemble-level 'scan ahead' activity of hippocampal place cells (Gupta et al., 2012; Johnson & Redish, 2007). Given the extensive analytical demands of the study, it is understandable that the authors chose to limit the analyses to the spatial and burst firing dynamics of the septal cells rather than the phasic firing of septal action potentials relative to local theta oscillations or CA1 theta oscillations. Yet, one would ideally be able to

link, rather than parse the phenomena of temporal dynamics. For example, Tingley et al recently showed that there was significant phase coding of action potentials in lateral septum cells relative to spatial location (Tingley & Buzsaki, 2018). This begs the question as to whether the non-uniform distribution of septal cell activity within the Y-maze may have a phasic firing component, as well as a theta cycle skipping component. If so, these phenomena could represent another means of information transfer within the spatial circuit during cognitive demands. Alternatively, these phenomena could be part of the same process, ultimately representing the coherent input of information from one region to another. Future experiments will therefore have to sort out whether theta cycle skipping, is a feature of either rate or phase coding, or perhaps both, depending on circuit and cognitive demands.

The authors have achieved their aims of describing the temporal dynamics of the lateral septum, at both the dorsal extreme and the intermediate region. All conclusions are warranted.